Wave and Turbulence Separation Using Dynamic Mode Decomposition

JULIO CHÁVEZ-DORADO,[a] ISABEL SCHERL,[b] AND MICHELLE DIBENEDETTO[a,c]

[a] *Department of Mechanical Engineering, University of Washington, Seattle, Washington*
[b] *Department of Mechanical and Industrial Engineering, University of Massachusetts, Amherst, Massachusetts*
[c] *Department of Mechanical and Aerospace Engineering, Princeton University, Princeton, New Jersey*

(Manuscript received 13 March 2024, in final form 9 January 2025, accepted 12 February 2025)

ABSTRACT: Separating the effects of waves and turbulence in oceanographic time series is an ongoing challenge because surface wave motion and turbulence fluctuations can occur at overlapping frequencies. Therefore, simple bandpass filters cannot effectively separate their dynamics. While more advanced decomposition techniques have been developed, they often entail restrictive assumptions about the wave and turbulence interactions, require synchronized measurements, and/or only decompose the signal spectrally without a time series reconstruction. We present our new wave–turbulence decomposition technique which uses dynamic mode decomposition (DMD). The technique is signal agnostic so it can be applied to any time series, and our only assumptions are that the waves and turbulence can be separated and that the waves are the most coherent features in the signal. Our approach requires minimal tuning, where the main user input is the wave frequency range of interest. To demonstrate the method, we apply it to synthetic, field, and laboratory data and compare the results to other modal decomposition methods. A sensitivity analysis on the synthetic data shows that the most sensitive parameter to the accuracy is the rank truncation in the DMD, and that the decomposition performs the best when the wave energy in the signal is of equal or greater magnitude than that of the turbulence. Given the accuracy of our decomposition, we are able to analyze the velocity autocorrelation of the separated turbulence time series with minimal wave contamination. Overall, our decomposition method outperforms the other decomposition methods and provides for robust separation of the waves and turbulence, demonstrating wide applicability to ocean signal processing.

SIGNIFICANCE STATEMENT: When measuring physical, chemical, and biological quantities in the ocean, the measurements are often influenced by both waves and turbulence. Isolating the individual effects of waves and turbulence on those variables is important to a wide range of analyses, such as estimating how momentum, heat, and nutrients are mixed throughout the water column. In this work, we propose a new method to separate the wave and turbulence components in ocean-data time series. When tested on laboratory, field, and synthetic data, our method was able to separate the wave and turbulence components of a signal more effectively than previously proposed algorithms.

KEYWORDS: Turbulence; Oceanic waves; Data science

1. Introduction

As observational advances increase the amount of ocean data available (Smith et al. 2019; Rosa et al. 2021), effectively interpreting and using this information, both in postprocessing and real-time analysis, is imperative for gaining insights into the dynamics of the ocean. One ongoing challenge is the interpretation of fluctuating data that are influenced by both turbulence and surface gravity waves. This is common in data obtained from the ocean surface and from the coastal ocean where both turbulence and surface waves are expected to be strong. Separating the turbulence and wave fluctuations in a signal is important for a variety of analyses: e.g., isolating the turbulence fluctuations in any signal is necessary for characterizing the turbulence Reynolds stress or for estimating a scalar eddy covariance flux. And isolating the wave motion is necessary, e.g., for quantifying wave energy or for wave energy control strategies (Li et al. 2012; Perez et al. 2020). We refer to this separation process as wave–turbulence decomposition.

The difficulties associated with wave–turbulence decomposition lie in the overlapping frequency domains where waves and turbulence exist—and that both can manifest as broadband signals with correlation in space and time. Even asserting that these signals can be effectively decomposed is an assumption, given the nonlinear interactions that can occur between waves and turbulence (Jiang et al. 1990; Magnaudet and Thais 1995; Guo and Shen 2013). Over the years, numerous methods have been developed to tackle this problem (Benilov et al. 1974; Jiang et al. 1990; Thais and Magnaudet 1995; Trowbridge 1998; Williams et al. 2003; Gerbi et al. 2008; Huang and Wu 2008; Young and Webster 2018; Bian et al. 2018). However, the various methods are usually adapted to the specific data at hand (Gerbi et al. 2008; Feddersen and Williams 2007; Jiang et al. 1990), involve restrictive assumptions (e.g., Benilov et al. 1974; Bricker and Monismith 2007), and/or require multiple and often complex synchronized measurements (Trowbridge 1998; Doron et al. 2001; Feddersen and Williams 2007). As a result, we still lack an effective, universal technique for decomposing a general time series.

Our goal is to develop a decomposition method that can be applied to a time series of any type of data. However, for simplicity, we will consider a velocity time series as it is the most

Corresponding author: Michelle DiBenedetto, mdiben@princeton.edu

DOI: 10.1175/JTECH-D-24-0039.1

commonly decomposed signal in this context. Consider the velocity decomposition:

$$u(x_i, t) = \langle u(x_i, t)\rangle + \tilde{u}(x_i, t) + u'(x_i, t), \tag{1}$$

where u is the instantaneous horizontal velocity, $\langle u\rangle$ is the time average, $\tilde{u}$ is the wave orbital velocity, and u' is the turbulence velocity fluctuation. In two dimensions, one result of Reynolds averaging the Navier–Stokes equations with this decomposition is the Reynolds shear stress:

$$-\frac{\tau}{\rho} = \langle \tilde{u}\tilde{w}\rangle + \langle \tilde{u}w'\rangle + \langle u'\tilde{w}\rangle + \langle u'w'\rangle. \tag{2}$$

The first term on the right-hand side is identically zero for irrotational waves described by linear wave theory but can be nonzero if the coordinate system is rotated, a common source of corrupted Reynolds stress measurements (Trowbridge 1998). The second and third terms are zero if there are no interactions between the waves and turbulence. The fourth term is the turbulence Reynolds shear stress, which is the only nonzero term as long as the aforementioned assumptions regarding linear wave theory and wave–turbulence interaction hold.

Spectral filtering techniques (Benilov et al. 1974; Bricker and Monismith 2007; Gerbi et al. 2008; Young and Webster 2018) are able to estimate bulk turbulence quantities like the Reynolds stress with some accuracy, but they do not allow for a time series reconstruction of the decomposed velocity signals because they are applied to the velocity power spectrum. Methods based on nonlinear streamfunctions (Dean 1965; Jiang et al. 1990; Thais and Magnaudet 1995, 1996) allow for a time-resolved separation with fewer assumptions but only work for specialized scenarios. More recent approaches involve dimensionality reduction techniques (Huang et al. 1998, 2009; Bian et al. 2018) that make use of mode decomposition to capture the coherent, oscillating nature of waves. However, it is common for these methods to remove turbulence energy in excess from the wave frequency range. In addition, these methods often require tuning parameters that lack a clear physical intuition. Nevertheless, dimensionality reduction techniques such as proper orthogonal decomposition (POD) (Lumley 1967), spectral POD (SPOD) (Towne et al. 2018; Schmidt and Colonius 2020), and dynamic mode decomposition (DMD) (Rowley et al. 2009; Schmid 2010) have become increasingly popular in fluid dynamics research due to their adaptability and effectiveness in extracting physically interpretable information from complex data. For example, POD has been used in pattern recognition in chaotic flows (Albidah et al. 2021), flow control (Gordeyev and Thomas 2013), and unsteady, high-Reynolds-number wake flows (Durgesh and Naughton 2010), and SPOD has been employed in diverse flows such as boundary layers (Tutkun and George 2017), mixing layers (Braud et al. 2004), wakes (Araya et al. 2017), and jets (Heidt and Colonius 2023), among others. Similarly, DMD is widely used in the study of wakes (Schmid 2010), jets (Schmid 2010; Seena and Sung 2011; Schmid 2011; Semeraro et al. 2012), instabilities (Duke et al. 2012; Grilli et al. 2012), and oscillations (Seena and Sung 2011; Massa et al. 2012; Albidah et al. 2021). However, these methods have yet to be applied to wave–turbulence decomposition, a problem for which they may be well suited. DMD shows promising filtering characteristics for an accurate wave–turbulence decomposition algorithm for single-point velocity measurements because it is designed to capture the time dynamics of coherent structures present in a signal.

Our approach is to develop a decomposition method that is as general as possible. We seek a signal-agnostic framework capable of handling one-dimensional time series data for a broad spectrum of flow parameters. Our methodology does not rely on severe assumptions about wave nor turbulence dynamics, making it adaptable to a variety of oceanic and environmental datasets. Thus, we will explore the effectiveness of DMD in a variety of datasets: synthetic data generated with no wave–turbulence interactions, field data collected in a swell-dominated bottom boundary layer, and laboratory data collected in a surface boundary layer under wind-generated waves. The remainder of the article has the following structure: Section 2 gives relevant background on other wave–turbulence decomposition methods and lays out the mathematical basis for the mode decomposition technique used in our proposed method. Section 3 outlines the procedure for our proposed decomposition method. In section 4, we describe the datasets used for validation, and we present the results of our decomposition in section 5, including both a sensitivity analysis and discussion. Finally, we summarize the study in section 6 and make suggestions for future work.

2. Background

a. *Wave–turbulence decomposition*

Wave–turbulence decomposition is a longstanding challenge that has been approached in a variety of ways. Simpler methods like moving average and bandpass filters are often used (Foster 1997; Smyth et al. 2002; Williams et al. 2003; Zhu et al. 2016) due to their ease of use and time-resolved output; however, these filters do not distinguish the waves from the turbulence in the overlapping frequency range, resulting in the elimination of turbulent energy.

Many spectral decomposition techniques have been developed that can estimate the Reynolds stress without allowing for a time series reconstruction; these methods often rely on the correlation between two separate measurements. For example, Benilov et al. (1974) proposed a linear filtration technique that leverages coherence between the pressure and velocity spectra. Similarly, Trowbridge (1998) and Shaw and Trowbridge (2001) proposed a method that leverages the coherence between two synchronized velocity measurements with a finite spacing. With only one velocity measurement, Bricker and Monismith (2007) proposed a method that linearly filters the energy spectrum by assuming an inertial subrange with a $-5/3$ slope, whereas Gerbi et al. (2008) proposed fitting the measured spectrum to an empirical spectrum model to separate the waves and turbulence. While these methods are also frequently used due to their relative simplicity, they assume no wave–turbulence interactions and do not directly allow for a reconstructed time series (unless further approximations are made, e.g., see Cowherd et al. 2021). Additionally,

some of the methods require multiple synchronized measurements which further restricts their use.

Some researchers sought a more rigorous characterization of the interaction of waves and turbulence by using the nonlinear wave streamfunction (Dean 1965), which imposed fewer assumptions and allowed for a time reconstruction of the filtered signal. Jiang et al. (1990) developed a method based on this work that consists of solving, in a least squares sense, the streamfunctions at the free surface. Similarly, the triple decomposition method from Thais and Magnaudet (1995, 1996) also used a streamfunction to decompose the instantaneous velocity into turbulent fluctuation, irrotational wave, and rotational wave components. Although these methods allow the construction of separate wave and turbulent velocity time series, they are most well suited to laboratory conditions where dispersive effects can be neglected (Thais and Magnaudet 1995).

More recently, data-driven dimensionality reduction techniques have been proposed to separate waves and turbulence. Ensemble empirical mode decomposition (EEMD) is the foundation of the method developed by Huang and Wu (2008). It is based on the empirical mode decomposition (EMD), which decomposes the signal into intrinsic mode functions (IMFs) which define a basis dictated by the data (Huang et al. 1998). While successful at separating a time series into different components, the method suffers because a single IMF can contain several oscillatory modes, or a single mode can be split into several IMFs. Huang and Wu (2008) proposed the EEMD to overcome this issue by introducing noise in the original signal to properly organize the different scales in the time series. The limitations of this improvement are that a large number of iterations are needed to remove the effects of the noise and obtain an accurate decomposition. In addition, ensemble averaging may affect the physical significance of the IMFs by artificially redistributing some energy among the IMFs. More recently, Bian et al. (2018) proposed the synchrosqueezed wavelet transform (SWT)-based method (Daubechies et al. 2011; Thakur et al. 2013), which decomposes the signal into a number of components separated in the time–frequency plane. This method forces the data to conform to a basis set determined a priori and tends to underestimate the turbulence in the wave frequency range. The EEMD and SWT are modal decomposition techniques that can be applied to a single time series and allow for a time-resolved signal reconstruction. For these reasons, we use them to compare the outputs of our DMD-based method in section 5.

To summarize, traditional decomposition methods applied in spectral space are limited to scenarios with no wave–turbulence interactions, often require specific assumptions and do not directly give a time series reconstruction. To address these limitations, methods based on modeling waves using streamfunctions were developed, but they are only effective under ideal conditions that are not commonly found in nature. Finally, newer modal decomposition methods have been successful in generating a time-resolved filtered signal, but they can have a significant impact on the turbulence in the wave frequency range.

b. Modal decomposition of flow data

In this section, we present a summary of relevant modal decomposition algorithms; for a more in-depth reference, see Schmid (2022). Modal decomposition refers to the identification and separation of modes, or patterns in data from a dynamical system. This type of decomposition is favorable because the general motion of a system, even nonlinear and nonstationary systems, can be approximated by a linear superposition of its modes. In the context of fluid dynamics, modal decomposition refers to the identification and separation of features in flow data. The singular value decomposition (SVD) is the basis for the implementation of several dimensionality reduction techniques such as POD (Lumley 1967) and DMD (Schmid 2010).

1) SVD AND POD

The SVD decomposes a matrix $\mathbf{M} \in \mathbb{R}^{m\times n}$ into the product of three matrices as follows:

$$\mathbf{M} = \mathbf{U}\boldsymbol{\Sigma}\mathbf{V}^{\mathrm{T}},$$

where $\mathbf{U} \in \mathbb{R}^{m\times m}$ and $\mathbf{V} \in \mathbb{R}^{n\times n}$ are unitary matrices and $\boldsymbol{\Sigma} \in \mathbb{R}^{m\times n}$ is a diagonal matrix with nonnegative real values. The singular values that make up the diagonal values $\sigma_k \in \boldsymbol{\Sigma}$ are in descending order and weight the modes. In other words, they are ordered based on how much of the total energy of the original data matrix they possess. The columns of $\mathbf{U}$ (expressed as $\mathbf{u}_k$) and the columns of $\mathbf{V}$ (expressed as $\mathbf{v}_k$) are known as the left singular vectors and right singular vectors of $\mathbf{M}$, respectively. A reduced-order approximation of the matrix $\mathbf{M}$ can be achieved by truncation as

$$\mathbf{M}_r \approx \sum_{k=1}^{r} \sigma_k \mathbf{u}_k \mathbf{v}_k^{\mathrm{T}},$$

where $\mathbf{M}_r$ is a rank r approximation of $\mathbf{M}$ using the $r \leq \min(m, n)$ most energetic singular modes.

The POD is simply an SVD applied to a specifically constructed $\mathbf{M}$ matrix. It was introduced in fluid mechanics by Lumley (1967, 2007), Sirovich (1987a,b,c), and Aubry et al. (1988). The matrix $\mathbf{M}$ is constructed as follows: given n snapshots of flow data in a discrete spatial grid of m points, each consecutive snapshot is reshaped into a corresponding column vector of a data matrix, $\mathbf{M} \in \mathbb{R}^{m\times n}$, where the kth column of $\mathbf{M}$, denoted as $\mathbf{x}_k$, contains all the spatial data of a singular snapshot at time $k\Delta t$ or, similarly, each row contains a time series of the flow data at a single point in space (Scherl et al. 2020). Thus, we obtain

$$\mathbf{M} = \begin{bmatrix} | & | & | & & | \\ \mathbf{x}_1 & \mathbf{x}_2 & \mathbf{x}_3 & \cdots & \mathbf{x}_n \\ | & | & | & & | \end{bmatrix}.$$

2) DMD

Dynamic mode decomposition (Schmid 2010) is used to determine the temporal periodicity of coherent structures present in flow data. DMD captures the system dynamics in the eigenvectors (modes) and eigenvalues of an infinite-dimensional linear operator, known as the Koopman operator.

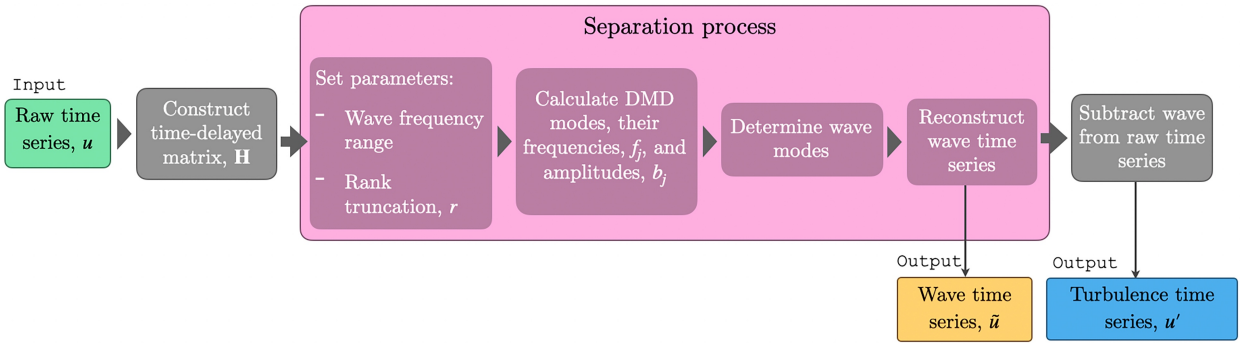

FIG. 1. Workflow of the proposed DMD wave–turbulence separation methodology.

DMD can separate system dynamics into modes that evolve over time. Additionally, DMD is tailored to recover oscillating dynamics without any prior knowledge of the system.

To compute DMD, one begins with n time steps of data across m dimensions. Each time step is shaped into a column vector of a present-state data matrix $\mathbf{X} \in \mathbb{R}^{m\times(n-1)}$ that contains time steps 1 to $n-1$, and a future-state data matrix $\mathbf{X}' \in \mathbb{R}^{m\times(n-1)}$ that contains time steps 2 to n. Thus, we have

$$\mathbf{X} = \begin{bmatrix} | & | & | & & | \\ \mathbf{x}_1 & \mathbf{x}_2 & \mathbf{x}_3 & \cdots & \mathbf{x}_{n-1} \\ | & | & | & & | \end{bmatrix} \quad \text{and}$$

$$\mathbf{X}' = \begin{bmatrix} | & | & | & & | \\ \mathbf{x}_2 & \mathbf{x}_3 & \mathbf{x}_4 & \cdots & \mathbf{x}_{n} \\ | & | & | & & | \end{bmatrix}.$$

Similar to POD, the kth column of either $\mathbf{X}$ or $\mathbf{X}'$, denoted as $\mathbf{x}_k$, contains all the data of a single time step at time $k\Delta t$ or, similarly, each row contains a time series of the data for a single dimension. The DMD algorithm attempts to find the best-fit linear operator $\mathbf{A}: \mathbf{X} \mapsto \mathbf{X}' \in \mathbb{R}^{m\times m}$ that advances the current state of the system $\mathbf{X}$ one time step into the future $\mathbf{X}'$ as

$$\mathbf{X}' \approx \mathbf{A}\mathbf{X}. \tag{3}$$

The solution to Eq. (3) can be approximated by a matrix $\mathbf{A}$ that minimizes $\|\mathbf{X}' - \mathbf{A}\mathbf{X}\|_F$ as

$$\mathbf{A} = \mathbf{X}'\mathbf{X}^{+}, \tag{4}$$

where $\|\cdot\|_F$ is the Frobenius norm and $\mathbf{X}^+$ is the pseudoinverse of the matrix $\mathbf{X}$. Instead of directly finding the pseudoinverse, the SVD of $\mathbf{X}$ yields $\mathbf{X} = \mathbf{U}\mathbf{\Sigma}\mathbf{V}^{\mathrm{T}}$ where $\mathbf{U}$, $\mathbf{\Sigma}$, and $\mathbf{V}$ are unitary and, therefore, can be used to express the pseudoinverse as $\mathbf{X}^{+} = \mathbf{V}\mathbf{\Sigma}^{-1}\mathbf{U}^{\mathrm{T}}$, which yields

$$\mathbf{A} = \mathbf{X}'\mathbf{V}\mathbf{\Sigma}^{-1}\mathbf{U}^{\mathrm{T}}, \tag{5}$$

where the eigenvalues and eigenvectors (DMD modes) of $\mathbf{A}$ capture the dynamics of the system. The eigenvalues of $\mathbf{A}$ are complex numbers that capture the growth/decay and oscillation of its corresponding DMD modes in their real and imaginary components, respectively. The DMD modes of $\mathbf{A}$ capture the spatial oscillatory patterns.

Typically, calculating $\mathbf{A}$ directly would be computationally intractable. Instead, a truncation of the matrices $\mathbf{U}$, $\mathbf{\Sigma}$, and $\mathbf{V}$ to retain only the first r singular values results in the reduced-rank matrices $\mathbf{U}_r$, $\mathbf{\Sigma}_r$, and $\mathbf{V}_r$ and yields a best-fit linear operator $\tilde{\mathbf{A}} \in \mathbb{R}^{r\times r}$ by projecting $\mathbf{A}$ onto the spatial modes $\mathbf{U}_r$ as follows:

$$\tilde{\mathbf{A}} = \mathbf{U}_r^{\mathrm{T}}\mathbf{A}\mathbf{U}_r = \mathbf{U}_r^{\mathrm{T}}\mathbf{X}'\mathbf{V}_r\mathbf{\Sigma}_r^{-1}. \tag{6}$$

The operator $\tilde{\mathbf{A}}$ has the same discrete-time eigenvalues $\mathbf{\Lambda}$ as $\mathbf{A}$. The eigenvectors $\mathbf{W}$ of $\tilde{\mathbf{A}}$ can be calculated as $\tilde{\mathbf{A}}\mathbf{W} = \mathbf{W}\mathbf{\Lambda}$ and converted to the high-dimensional eigenvalues $\mathbf{\Phi}$ of $\mathbf{A}$, as follows (Tu et al. 2014):

$$\mathbf{\Phi} = \mathbf{X}'\mathbf{V}_r\mathbf{\Sigma}_r^{-1}\mathbf{W}. \tag{7}$$

From the leading eigenvalues $\mathbf{\Lambda}$ and eigenvectors $\mathbf{\Phi}$, the solution of the system can be recreated as

$$\mathbf{X} = \mathbf{\Phi}\exp(\mathbf{\Omega}t)\mathbf{b} = \sum_{k=1}^{r} \phi_k \exp(\omega_k t) b_k, \tag{8}$$

where $\mathbf{\Omega} = \log(\mathbf{\Lambda})/\Delta t$ is the continuous-time eigenvalue of $\mathbf{A}$ and $\mathbf{b} = \mathbf{\Phi}\backslash\mathbf{X}(t_0)$ is the initial condition of the system.

3. Methods

Figure 1 shows a diagram summarizing the algorithm workflow, which is described below. For the method we propose, the input matrix contains a one-dimensional time series of discrete, pointwise flow measurements such as one velocity component (u, v, or w), or other variables like water elevation, scalar concentration, pressure, etc. These measurements are collected at a sampling frequency f_s over a specified duration T, for $N = Tf_s$ total observations in the given time series. Our approach is to use DMD to extract the most coherent features of the signal, which we assume to be the waves, as low-rank structures and subtract them from the raw signal to isolate the turbulence. Although other order-reduction techniques exist, they have limitations. For example, POD identifies correctly the rank of the system, but since this method is based entirely on energy (or contained variance), the modes are not temporally orthogonal. In other words, POD can hierarchically rank

coherent features in the signal based on their energy content, but it cannot offer insights into how these patterns evolve over time. This is not ideal for our problem because we expect waves to be represented as modes that have coherent oscillations in time. In contrast, DMD can separate the dynamics in the system and can identify their temporal oscillation frequency. This allows us to identify a specific frequency per mode that we can associate with wave motion (Kutz et al. 2016).

In frequency space, waves can be narrow banded when compared with turbulence, but their energy can still span over multiple orders of magnitude in frequency. The broader the wave frequency range, the larger the number of DMD modes will be needed to represent the waves. However, the number of modes that DMD can extract is limited by the rank of the input data matrix. Because we want to extract a range of wave modes, we need to increase the rank of our time series before we apply DMD.

Hence, we propose to address this problem and increase the rank of the input data matrix by constructing a delay embedding of the time series signals, i.e.,

$$\mathbf{H} = \begin{bmatrix} x_1 & x_2 & x_3 & \cdots & \cdots & x_n \\ x_2 & x_3 & & & & \vdots \\ x_3 & & & & & \vdots \\ \vdots & & & & & x_{N-2} \\ \vdots & & & & x_{N-2} & x_{N-1} \\ x_m & \cdots & \cdots & x_{N-2} & x_{N-1} & x_N \end{bmatrix}, \tag{9}$$

where $m = N - n$ is the number of time lags and n is the number of columns. Note that the matrix $\mathbf{H}$ can have multiple rows besides the time-delay process if one has multiple data series (e.g., see Filho and Lopes dos Santos 2019; Fujii et al. 2019; Lydon et al. 2025). The introduction of the time delay serves a crucial role in increasing the rank of the data by increasing the "information" content of the matrix (Takens 1981). Physically, this increase in rank can be analogous to Taylor's frozen turbulence hypothesis, since the time observations of the signals are converted to spatial observations.

To filter the signal using DMD, we first need to determine the wave frequency range, the dimension of the time-delayed matrix $\mathbf{H}$, and the rank truncation r. Visual inspection of the signal's power spectrum helps determine the wave frequency range by identifying the points where the wave peak meets the expected turbulence energy spectrum. For the construction of the time-delayed matrix, the number of columns n needs to be large enough to capture the lowest wave frequencies of interest in each row. Based on our sensitivity analysis described below, we find that a good rule of thumb is within the range $n/N \approx [1/3, 1/2]$; however, in our data, the decomposition is not as sensitive to this parameter as it is to the rank truncation r, especially given a sufficiently long time series. In general, we suspect that this parameter might require some tuning to determine the appropriate dimensions of $\mathbf{H}$. From this new configuration $\mathbf{H}$ of the input data, the present and future-state matrices $\mathbf{X}$ and $\mathbf{X}'$ are constructed as indicated in section 2 as input for the DMD algorithm. To determine the rank truncation r, we perform a POD decomposition of $\mathbf{H} = \mathbf{U}_H \mathbf{\Sigma}_H \mathbf{V}_H^{\mathrm{T}}$ and compute the spectral density of each column $\mathbf{v}_j \in \mathbf{V}_H$ (known as time expansion coefficients) as $\mathbf{C}_j = |\mathscr{F}\{\mathbf{v}_j\}|^2/(f_s N)$, where $\mathscr{F}\{\cdot\}$ is the Fourier transform operator. The vector $\mathbf{C}_j$ contains the energy content at each frequency of the jth POD mode of $\mathbf{H}$ (Towne et al. 2018). Plotting the energy content of each singular value mode $\mathbf{C}$ as a function of frequency helps us visualize which modes contain wave and/or turbulence energy. Next, we identify and discard the highest modes that do not contain wave energy. The parameter r consists of the lowest modes that contain wave energy. This truncation allows us to remove the higher-frequency turbulence from the data directly.

DMD is then applied to $\mathbf{H}$, using the rank truncation r that we just determined. Following the procedure outlined in the previous section, we obtain the eigenvalues $\mathbf{\Lambda}$, eigenvectors (or modes) $\mathbf{\Phi}$, and amplitudes $\mathbf{b}$, which capture the coherent structures in the matrix $\mathbf{H}$. The jth DMD mode ϕ_j and its corresponding eigenvalue λ_j have a distinct oscillation frequency f_j that can be calculated as

$$f_j = \frac{\mathrm{Im}[\log(\lambda_j)]}{2\pi\Delta t}. \tag{10}$$

The modes with frequencies within the wave range are referred to as wave modes and are transformed to the time domain as a wave time series using Eq. (8). The wave time series is then subtracted from the raw signal, leaving the turbulence component of the signal.

4. Dataset descriptions

We test our method on three distinct datasets to show its broad applicability: a synthetic dataset with known wave and turbulence components, a field dataset collected on a swell-dominated coastal shelf in a bottom boundary layer published in Reimers and Fogaren (2021), and laboratory data we collected in a surface boundary layer in a wind-driven wave tank. Table 1 shows some flow and DMD parameters used in our proposed decomposition method for each dataset. Additionally, it shows the relative wave intensity $\tilde{u}_{\mathrm{rms}}/u'_{\mathrm{rms}}$, which is estimated as the ratio of the wave to the turbulence root-mean-square velocity obtained from the DMD-based decomposition. Note that we cover a range of wave intensities, and that the field and laboratory waves are the most and least intense, respectively.

a. Synthetic data

Synthetic data allow us to test our wave–turbulence decomposition by comparing our decomposed velocities to the ground-truth signals directly. To create the dataset, we linearly add a wave $\tilde{u}$ and turbulence u' velocity time series. In this case, wave–turbulence interactions are exactly zero and $\tau/\rho = -\langle u'w' \rangle$. The turbulence data come from a streamwise velocity time series collected with hot-wire anemometry in a wind tunnel sampled at 60 kHz (Castro and Vanderwel 2021). The turbulence spectrum has a developed inertial range between 0.13 and 0.6 Hz.

TABLE 1. Summary of dataset characteristics including some input and output parameters from the wave–turbulence decomposition. Characteristics include length of time series N, sampling frequency f_s, wave peak period T_p, and wave frequency range. We also report the optimal number of rows m and columns n of the time-delayed matrix $\mathbf{H}$, the optimal rank truncation r used, and the number of wave DMD modes ψ_{wave}, including the relative rank r/n used to separate high-frequency turbulence unaffected by the wave and ψ_{wave}/r used to reconstruct the wave time series. The final column reports the relative wave intensity $\tilde{u}_{\text{rms}}/u'_{\text{rms}}$ using the DMD-separated velocities. For the synthetic data, the true wave intensity is $\tilde{u}_{\text{rms}}/u'_{\text{rms}} = 1.81$.

Data type	N	f_s (Hz)	T_p (s)	Wave range (Hz)	m	n	r	ψ_{wave}	r/n	ψ_{wave}/r	$\tilde{u}_{\text{rms}}/u'_{\text{rms}}$
Synthetic	10 000	10	5	0.117–0.6	3000	5911	173	104	0.029	0.601	1.91
Field	7200	8	14.29	0.031–0.175	5700	1500	48	34	0.027	0.708	8.05
Laboratory, u	18 000	30	0.5	1.02–3.16	13 000	5000	1000	506	0.200	0.506	0.30
Laboratory, w	18 000	30	0.5	1.02–3.16	12 500	6500	1300	732	0.200	0.563	0.72

The wave amplitude spectrum $S(\omega)$ was generated using a Joint North Sea Wave Project (JONSWAP) model (Hasselmann et al. 1973) as follows:

$$S(\omega) = \frac{\alpha g^2}{\omega^5}\exp\left[-\frac{5}{4}\left(\frac{\omega_p}{\omega}\right)\right]\gamma^{\exp[-(\omega/\omega_p-1)^2/2\beta^2]}, \tag{11}$$

where $\alpha = 0.01$ is the intensity of the JONSWAP spectrum, g is the acceleration of gravity, ω is the angular frequency, ω_p is the angular frequency of the peak of the spectrum, $\gamma = 3.3$, and the factor $\beta = 0.07$ for $\omega \leq \omega_p$ and $\beta = 0.09$ for $\omega > \omega_p$. The peak period T_p was chosen to be 5 s, which results in $\omega_p = 1.26$ rad s^{-1}. At a point below the surface where $x = 0$ and $z = -2$ m, linear wave theory was used to generate the velocity time series from the sum of $N_w = 500$ wave components:

$$\tilde{u}(x, z, t) = \sum_{i=1}^{N_w} \mathbf{U}_i \cos(k_i x - \omega_i t + \phi_i)\exp(k_i z), \tag{12}$$

where $\mathbf{U}_i = a_i\omega_i$ is the wave velocity amplitude vector, $a_i = \sqrt{2S(\omega_i)d\omega}$ is the amplitude of the spectrum at frequency ω_i, $k_i = \omega_i^2/g$ is the wavenumber that satisfies the deep-water linear dispersion relation, and ϕ_i is the phase which is randomly sampled from the interval $[0, 2\pi)$.

The turbulence time series was decimated from 60 kHz to 10 Hz to match the sampling frequency of the JONSWAP waves time series. The total detrended horizontal component of velocity u is obtained from adding the wave and turbulence components of horizontal velocity, defined in Eq. (1), as $u = u' + \tilde{u}$. The power spectrum of u, shown in Fig. 2b, preserves the turbulence developed inertial range between 0.13 and 0.6 Hz and shows that the wave energy is concentrated around the wave peak frequency at 0.2 Hz.

b. Field data

The field data consist of long waves measured in a turbulent boundary layer above the coastal shelf. The data come from a published dataset in Reimers and Fogaren (2021). We are analyzing their acoustic Doppler velocimeter (ADV) data collected during a campaign to measure oxygen eddy covariance. The ADV captures a time series of the three perpendicular velocity components and pressure at a single point in space. We analyze only a time series of u velocity components from their data. The measurements were collected from a lander deployment along the Oregon shelf above a sandy seafloor. The ADV probe's sampling volume was 30 cm above the bottom of the sea floor in 80 m of water and was sampling at a frequency of $f_s = 64$ Hz, which was then downsampled to $f_s = 8$ Hz. Each deployment was broken down into 15-min (7200 observations) long bursts, and we consider only one burst in our study. The mean current of the analyzed burst time series is 0.11 m s^{-1}, the peak wave period T_p is 14.28 s (see Fig. 8b), and for reference, the significant wave height was estimated to be 3.4 m. We chose this specific burst because it presented a mix of high and low amplitude waves, as shown in Fig. 8c. For further details about the data acquisition, please consult the original study (Reimers and Fogaren 2021).

c. Laboratory data

To contrast the bottom boundary layer field data, we collected laboratory data in a wind-driven surface boundary layer with short intermittently breaking waves. The data were collected during experiments conducted in the Washington Air–Sea Interaction Facility (WASIRF) which is a 12.2-m-long, 0.91-m-wide wind-wave tank. Freshwater was filled to a depth of 0.6 m leaving 0.6 m of headspace above for air circulation. To create wind, a suction fan propelled air through the test section's headspace and recirculated it via an overhead duct. See Baker and DiBenedetto (2023) for more details on the facility.

We collected a time series of three-dimensional velocity at a height of 19 cm below the water surface with an ADV (Nortek Vectrino) under a wind speed of 16 m s^{-1} at a fetch of 7.5 m. The data were collected over 20 min at a sampling frequency $f_s = 30$ Hz. The wave energy spans the frequency range of 1–3 Hz, with a peak at 2 Hz (Figs. 9b and 10b). We postprocessed the data using the despiking method proposed by Goring and Nikora (2002). Even after despiking the data, there is still some noise present in the data due to intermittent wave breaking which generated bubbles which affected the data quality. These noisy data provide another challenge to the decomposition. We apply our decomposition method to both the horizontal and vertical components of velocity because they present contrasting conditions. The horizontal velocity data have high turbulence fluctuations when compared to the wave velocities, whereas the vertical velocity has wave and turbulence fluctuations with similar magnitude (see Table 1). Finally, we note that due to the strong anisotropy in the surface boundary layer flow, we see deviation from the −5/3 slope in the inertial range (Fig. 9b).

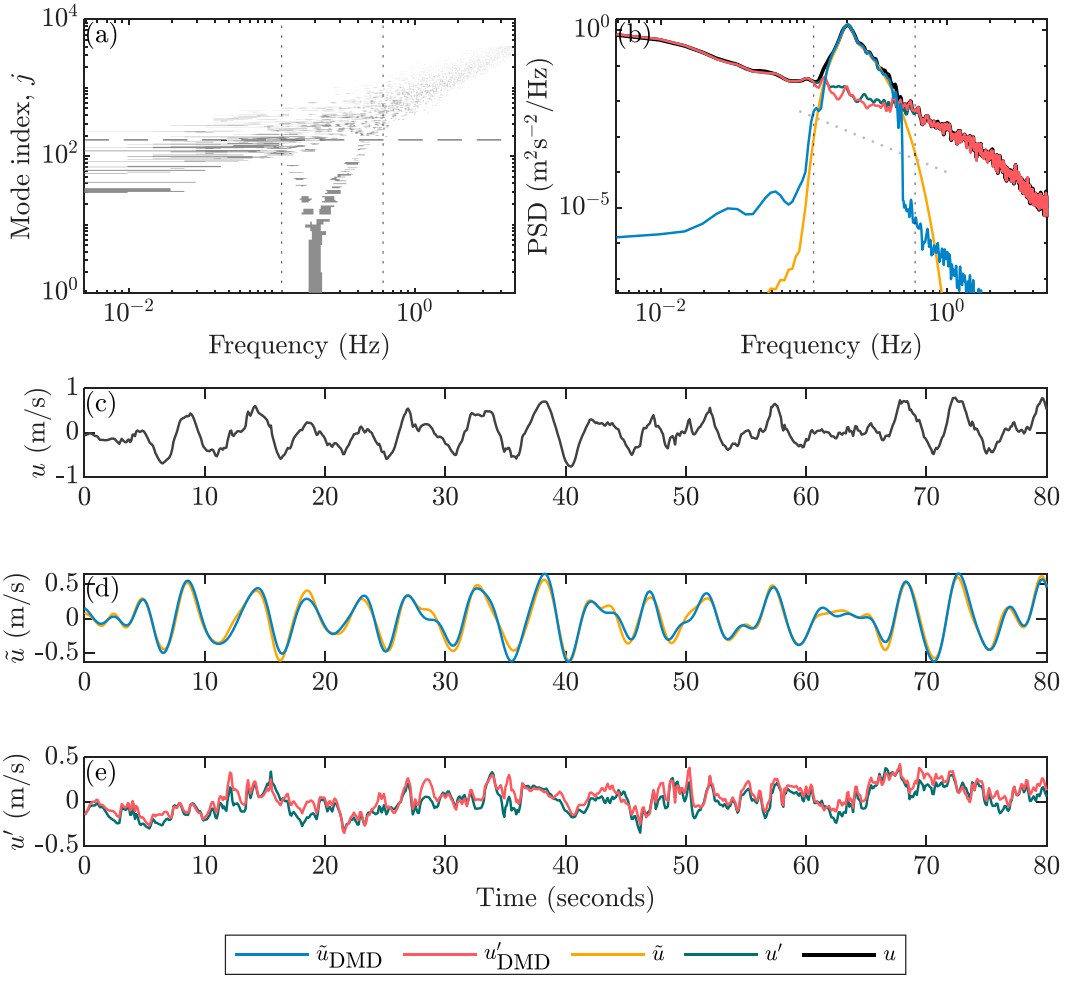

FIG. 2. DMD wave–turbulence decomposition of u-component velocity of synthetic data. (a) POD spectrum of time-delayed matrix **H**. (b) Power spectra of the original data and DMD-separated wave and turbulence. A gray −5/3 slope line is plotted for reference. (c) A portion of the original time series; (d) the true and separated wave components using 104 DMD modes; and (e) the true and separated turbulence components.

5. Results and discussion

In this section, we present the results obtained from analyzing the synthetic, laboratory, and field data with our proposed DMD method. We demonstrate our DMD decomposition by applying it to all three datasets after first conducting a sensitivity analysis on the synthetic data. Next, we compare our results to the other two time-resolved mode-based decomposition methods: EEMD (Qiao et al. 2016; Huang et al. 2009) and SWT (Bian et al. 2018). After assessing the decomposition in both spectral and time space, we analyze the temporal autocorrelation of the decomposed turbulence signal, further demonstrating how our DMD method outperforms the other methods.

a. Synthetic data decomposition

The first step of our decomposition method is constructing the time-delayed matrix **H** and identifying the wave frequency range, as described in section 4 and reported in Table 1. Next, we determine the rank truncation r by plotting the POD spectrum of **H** of the synthetic u data (Fig. 2a) and selecting the modes that contain wave energy. We observe two strong features in this plot: 1) the higher modes contain energy in monotonically increasing frequencies across the entire domain due to turbulence, showing the energy decreasing from low to high frequencies consistent with the inertial range, and 2) a coherent high-energy signal in lower modes between the frequency range of 0.13 and 0.6 Hz indicated by the vertical dotted lines. This "dip" in the POD spectrum indicates an energetic range associated with the wave energy and accounts for a significant part of the variance in the time series. We use the location of the dip to inform the rank truncation. As indicated with the horizontal dashed line, we truncate at the $r = 173$ mode; that is, we take only the first 173 modes for the next step in the DMD. We see that while most of the wave energy is contained in these first r modes, there is also energy associated with low-frequency turbulence in these lowest modes. This clearly shows how POD alone fails at separating waves

and turbulence since it can only isolate the high-frequency turbulence from the waves, not the lower-frequency turbulence.

After determining the rank truncation, we are able to decompose the signal using DMD. Figure 2b shows the spectra of the DMD-filtered wave and turbulence time series which we compare with the true wave and true turbulence spectra. Within the wave frequency range, the DMD-filtered wave spectrum $\tilde{u}_{\mathrm{DMD}}$ closely follows the wave peak. Outside the wave frequency range, the $\tilde{u}_{\mathrm{DMD}}$ spectrum falls sharply, capturing a similar shape to the true wave spectrum for multiple orders of magnitude before levelling off. The mismatch in the signals is clearer to see in the u'_{DMD} spectrum, which slightly underpredicts the turbulence in the wave frequency range.

Figures 2c–e show a portion of the u time series and the decomposed $\tilde{u}$ and u' time series alongside their true counterparts. We see overall agreement between the decomposed and true time series; however, some mismatch exists. While the turbulence time series plot shows that the separated signal accurately captures the low-frequency turbulence fluctuations, there is stronger disagreement in the fluctuations with frequencies in the wave range. Given that the wave signal was generated with 500 discrete wave signals and that the DMD only resolved 104 modes, we do not expect a perfect reconstruction. In this method, the DMD is discretizing a wave frequency range that in reality is continuous, so we always expect some mismatch. The column r/n in Table 1 shows the ratio of the number of modes used to truncate the input matrix normalized by the number of columns used to construct the input matrix. For the synthetic data, the low rank-to-column ratio indicates that the dominant wave patterns in the signal were reconstructed using fewer modes compared to the other datasets.

1) Sensitivity analysis on decomposition parameters

We conducted a sensitivity analysis on the decomposition based on the two main tuning parameters: the rank truncation r and the number of columns of the time-delayed input matrix n to identify the optimal r_{opt} and n_{opt} for the decomposition. In addition, we also varied the length of the time series N and repeated the sensitivity analysis to assess how r and n vary with N. We quantified the accuracy of the decomposition by calculating the normalized error ϵ, which is defined as follows:

$$\epsilon = \frac{\|u'_i - u'_{i,\mathrm{DMD}}\|_2}{\|u'\|_2}, \tag{13}$$

where u'_i and $u'_{i,\mathrm{DMD}}$ are the true and decomposed turbulence time series (here the notation refers to DMD, but we also calculate this error for the EEMD and SWT methods), respectively, at time t_i, and $\|\cdot\|_2$ is the L_2 norm. For comparison, we also measured the mean absolute error α defined as

$$\alpha = \frac{1}{N}\sum_{i=0}^{N} |(u'_i - u'_{i,\mathrm{DMD}})|. \tag{14}$$

We conduct the sensitivity analysis across four different time series lengths to assess the importance of the length of the dataset. Figures 3a–d show the results of the sensitivity analysis for $N = 10\,000$, 7500, 5000, and 2500, respectively. We plot the norm-based error ϵ for different combinations from the space of normalized r/n_{opt} and normalized number of columns n/N. The optimal combination (n_{opt}/N, $r_{\mathrm{opt}}/n_{\mathrm{opt}}$) is indicated by a red cross.

Overall, the optimal n/N ratio is not too sensitive and ranges between 0.5 and 0.6, while the optimal r minimizes the error only in a narrow range of values. This indicates that, at least for this simple case, the preferential dimension of the input time-delayed matrix is an approximately square matrix. This might be due to the fact that for a large dataset, we have enough physical information to resolve coherent features in the time domain n and the "spatial" domain m that we constructed via time delaying. However, when there is limited information by the shortened time series, as in the case of Fig. 3d, the preferential input matrix shape is a tall, skinny matrix. This suggests a preference for spatial information over temporal information and that meeting a critical column length is more important than increased row length. We can observe that the optimal r shows a small decrease with N (except for $N = 2500$) but overall is fairly stable. Selecting an appropriate rank truncation is essential for accurately capturing the waves in the time series. If r is too low, some waves may be missed by the DMD algorithm, leading to an incomplete reconstructed time series. Conversely, if r is too high, it may lead to overestimation of the wave energy.

Table 2 summarizes the different tuning parameters for all time series length N and their associated errors. We see a decrease of the norm-based error ϵ with N which makes sense since the DMD is a data-based algorithm, and more data generally improve performance. However, as the data increase so does the computational cost of performing the decomposition. We compare the DMD method to EEMD and SWT in Table 2, where we see that given the same time series length, our DMD method outperforms the other modal decomposition methods. While the EEMD outperforms the SWT, they both have higher errors than the DMD method, even when DMD was applied to only half the data ($N = 5000$). Overall, our method seems to perform the best when applied to this dataset. At the end of this section, we compare the methods in more detail by applying them to all of the datasets.

In our analysis, we use the ratio r/n to understand how effectively the first step of our algorithm, the rank truncation, separates waves from turbulence. A low r/n indicates a more effective rank truncation. This ratio measures how well we can isolate the wave energy from the higher-frequency turbulence that does not overlap in the frequency space. Essentially, this step resembles a low-pass filter, in the sense that most of the truncated modes correspond to high-frequency motion. We do not expect r/n to be universal because the shape of the spectra can vary; e.g., narrow-banded waves at lower frequencies would likely result in a lower r/n relative to wide-banded waves with the same intensity that occupy higher frequencies, given the same turbulence spectrum. In addition, the number of columns n in the input matrix controls the lowest resolvable frequencies and, therefore, will depend on the location of the wave frequency peak in frequency

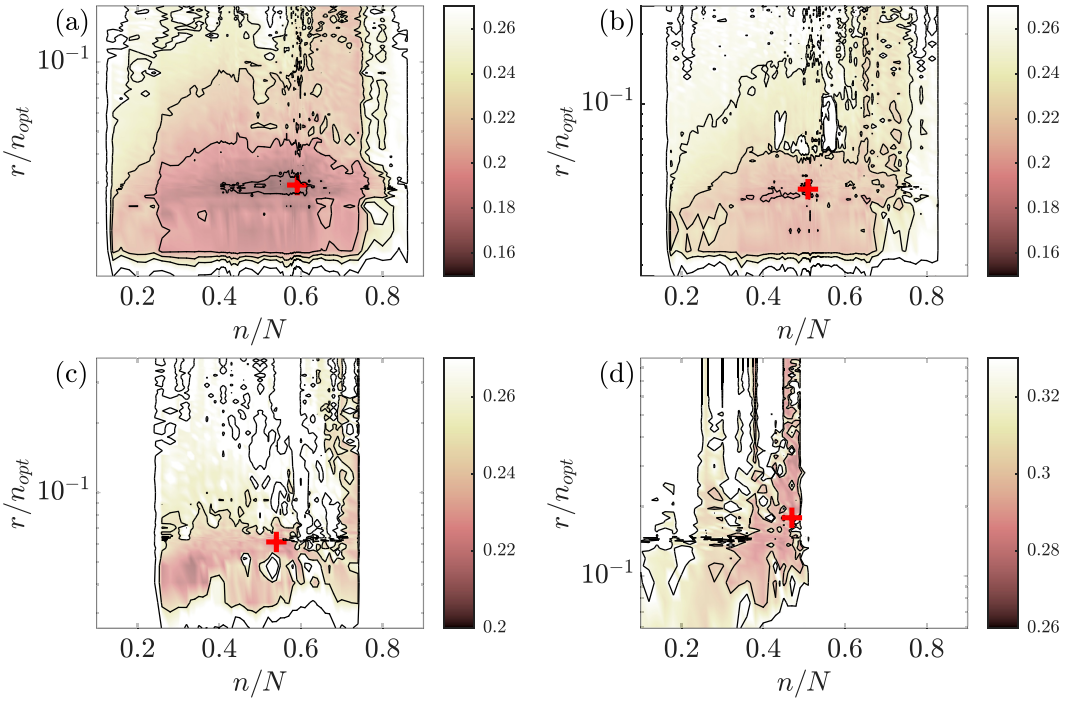

FIG. 3. Sensitivity analysis to assess the separation performance of the DMD-based algorithm for different time series lengths N. A measurement of error ϵ was calculated for every combination of normalized rank truncation r/n_{opt} and normalized number of columns n/N in the time-delayed matrix $\mathbf{H}$, where n_{opt} is the optimal number of columns and the optimal combination is indicated by a red cross. The (a) $\epsilon = 0.1586$, at $r_{\text{opt}}/n_{\text{opt}} = 0.029$, $n_{\text{opt}}/N = 0.5911$ ($N = 10000$); (b) $\epsilon = 0.1894$, at $r_{\text{opt}}/n_{\text{opt}} = 0.043$, $n_{\text{opt}}/N = 0.509$ ($N = 7500$); (c) $\epsilon = 0.2109$, at $r_{\text{opt}}/n_{\text{opt}} = 0.061$, $n_{\text{opt}}/N = 0.540$ ($N = 5000$); and (d) $\epsilon = 0.2737$, at $r_{\text{opt}}/n_{\text{opt}} = 0.179$, $n_{\text{opt}}/N = 0.470$ ($N = 2500$).

domain; higher-frequency waves might require a smaller n compared to low-frequency waves to capture the peak wave frequency. Our observations show that r/n generally increases as wave intensity decreases, indicating that the rank truncation is less effective at isolating wave energy when the waves are weaker.

We next consider ψ_{wave}/r to evaluate the effectiveness of the second step of our decomposition (see Table 1). This ratio represents the proportion of DMD modes used to reconstruct the waves relative to all modes remaining after the initial truncation. Higher wave intensity usually corresponds to a higher ψ_{wave}/r because most of the modes retained are wave modes. Essentially, to summarize the two main steps of the algorithm: first, the rank truncation initially identifies the modes containing the relevant frequency content, and second, the DMD step extracts the wave components from this subset. By quantifying r/n and ψ_{wave}/r, we can compare the effectiveness of each step in the separation process.

2) SENSITIVITY ANALYSIS ON WAVE INTENSITY

Additionally, we performed a sensitivity analysis on the effect of relative wave intensity $\tilde{u}_{\text{rms}}/u'_{\text{rms}}$. We scaled the synthetic wave time series amplitudes linearly to adjust the wave intensity, keeping the frequency and phase components of the synthetic wave signal constant. This results in the wave spectrum moving up or down relative to the turbulence spectrum, as shown in Fig. 4. This also changes the apparent width of the wave spectral peak which overlaps the inertial range, a change that is due to the weaker wave energy away from the peak frequency being overshadowed by the turbulence. We chose the wave intensities $\tilde{u}_{\text{rms}}/u'_{\text{rms}} = [0.2, 0.5, 1, 5, 10]$, in addition to the wave intensity $\tilde{u}_{\text{rms}}/u'_{\text{rms}} = 1.81$ that we used in the previous single-case analysis (Fig. 2), to cover a wide range of scenarios. This range also covers the high and low intensities present in the field and laboratory data, respectively.

Figure 5 presents the norm-based reconstruction errors for waves and turbulence across varying wave intensities. We expect a decrease in the reconstruction error as wave intensity increases because the DMD algorithm will be able to more effectively identify the coherent features of wave motion as distinct from the turbulence. Conversely, as wave intensity decreases, the performance of our decomposition method is expected to decline. We note that the error in turbulence reconstruction decreases more slowly with increasing wave intensity, relative to the wave reconstruction error. This is because the turbulence reconstruction is less sensitive to the decomposition because most of the turbulence in the signal is unaffected by the waves due to it occurring at frequencies outside the wave range.

In Fig. 6, we plot the decomposed wave spectra relative to the input spectra and the true wave spectra to further evaluate the effectiveness of the decomposition. We see that in all

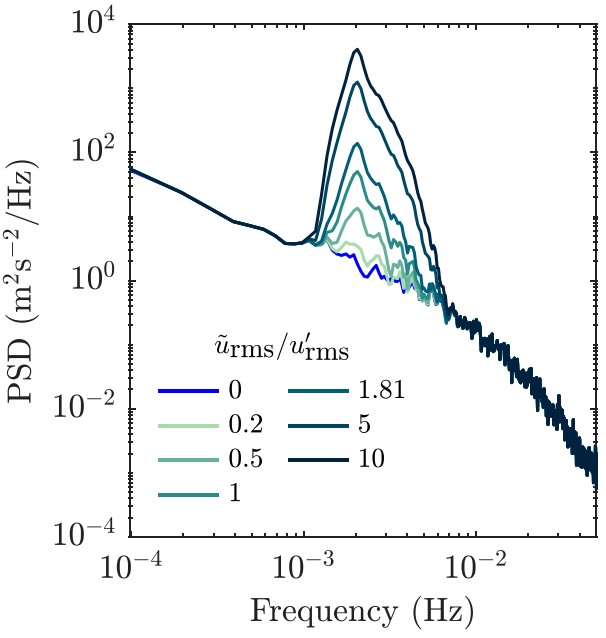

FIG. 4. Synthetic spectra used for sensitivity analysis on wave intensity $\tilde{u}_{rms}/u'_{rms}$. Wave intensity of zero represents the raw turbulence signal u'.

cases, the wave peak above the turbulence spectra is well represented by the decomposition. However, as the wave intensity decreases and more of the wave spectrum falls below the turbulence spectrum, we see that the decomposition struggles to recover the shape of the original wave spectrum accurately. This is especially clear in the lowest wave intensity case, which has a large wave reconstruction error due to the poor reconstruction of the wave and the small norm of the true wave signal. Additionally, we see that the DMD method tends to overestimate the wave energy at the lower end of the wave frequency range, while underestimating the wave energy at the higher end. However, these errors are small compared to the overall spectral energy in the combined wave and turbulence signal. In summary, the DMD method works best when the wave intensity is high and fails when the wave intensity is low; therefore, we recommend our method for cases when the wave energy is similar or larger in magnitude than that of the turbulence and for when there exists a clear wave peak in the power spectrum of the raw signal.

To further evaluate how the decomposition performs across wave intensity, we consider the relative energy of the DMD wave modes. Figure 7 shows a direct correlation between the amount of wave energy in the signal and the corresponding DMD mode energy required to accurately reconstruct the wave signal. The expression $\sum|b_{wave,i}|^2/\sum|b_i|^2$ in the y axis in Fig. 7 quantifies the ratio of the energy contributed by the subset of wave-containing DMD modes to the total energy from all DMD modes. Values close to unity mean that the wave modes dominate the dynamics of the system, while values close to zero mean that the contribution of the wave

TABLE 2. Summary of sensitivity analysis from Fig. 3 (top), and comparison of errors from DMD and other modal decomposition methods applied to the longest time series length of $N = 10\,000$ (bottom).

	Length of raw time series, N			
Parameters	2500	5000	7500	10 000
r_{opt}	210	165	155	173
r_{opt}/n_{opt}	0.179	0.061	0.043	0.029
n_{opt}	1175	2700	3900	5911
n_{opt}	0.47	0.54	0.52	0.59
ϵ	0.2737	0.2109	0.1894	0.1586

Method	ϵ	α (m s^{-1})	α/u'_{rms}
DMD	0.159	0.039	0.24
EEMD	0.268	0.065	0.40
SWT	0.325	0.079	0.49

modes is small compared to the overall dynamics. Figure 7 also shows a general trend across datasets and wave intensities. When waves and turbulence are similar in intensity ($\tilde{u}_{rms}/u'_{rms} = 1$), the waves account for approximately half of the energy in the DMD modes. However, as the wave intensity nearly doubles ($\tilde{u}_{rms}/u'_{rms} = 1.81$), the proportion of DMD mode energy associated with waves increases significantly, indicating a strong dominance of wave energy in the reconstruction. Conversely, when the wave intensity is halved, waves contribute only about 30% of the DMD mode energy, highlighting the reduced influence of weaker wave signals.

b. *Field data decomposition*

We plot the POD spectrum of the field data (Fig. 8a) and find that, similar to the synthetic data in Fig. 2a, there are two

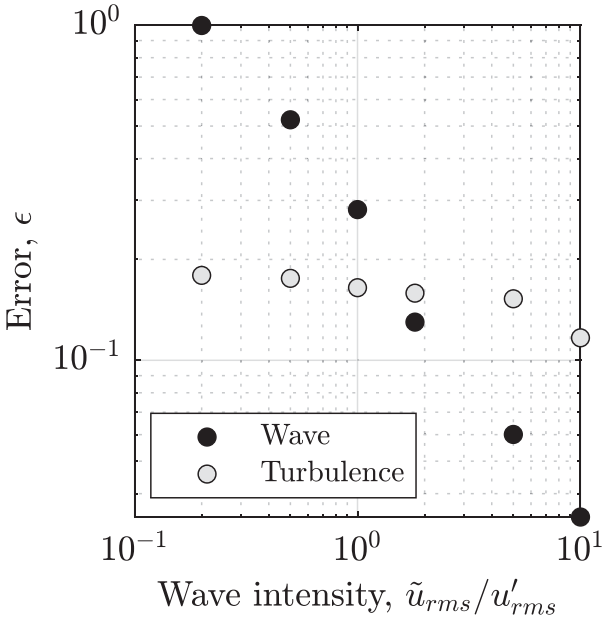

FIG. 5. Reconstruction error from wave and turbulence at the different wave intensities in the sensitivity analysis.

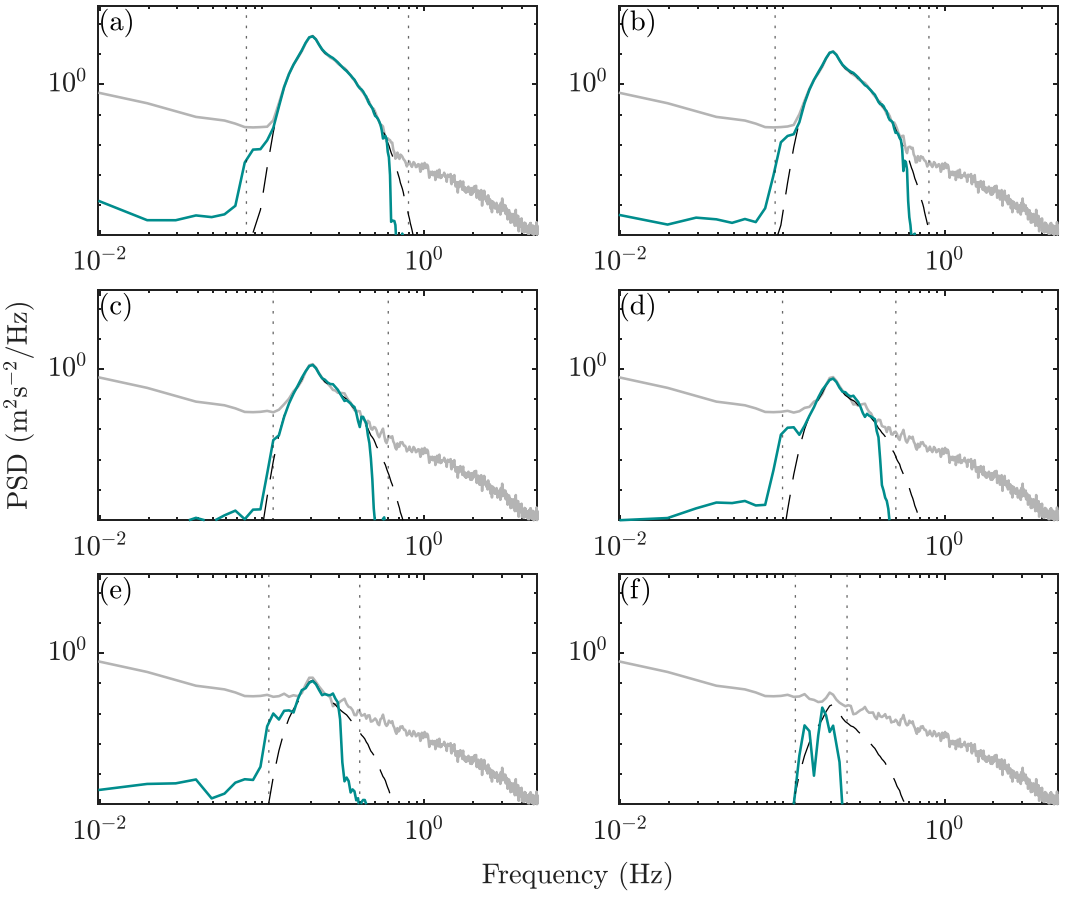

FIG. 6. Comparison of the DMD-separated wave spectrum (solid teal line) to the true wave spectrum (dashed black line) and the combined wave and turbulence spectrum (solid gray line). Each subfigure corresponds to a wave intensity: (a) $\tilde{u}_{\text{rms}}/u'_{\text{rms}} = 10$, (b) $\tilde{u}_{\text{rms}}/u'_{\text{rms}} = 5$, (c) $\tilde{u}_{\text{rms}}/u'_{\text{rms}} = 1.81$, (d) $\tilde{u}_{\text{rms}}/u'_{\text{rms}} = 1$, (e) $\tilde{u}_{\text{rms}}/u'_{\text{rms}} = 0.5$, and (f) $\tilde{u}_{\text{rms}}/u'_{\text{rms}} = 0.2$.

features: one associated with the turbulence energy that is seen across the frequency range and one that marks a dip in the energetic modes associated with the wave energy concentrated between 0.03 and 0.2 Hz, demarcated with the vertical dotted lines. It is worth noting that in this case, there is not a well-defined turbulence signal in the wave frequency range. Wave and turbulence interactions present in real data, as compared with the synthetic data, may reduce the effectiveness of the POD modal separation in the overlapping frequency range. This further supports why POD alone cannot always isolate waves and turbulence. Based off the location of the dip, we rank truncate to $r = 48$ modes to preserve the energy in the wave frequencies and remove the high-frequency turbulence. The final filtered velocity spectra are shown in Fig. 2b alongside the raw signal spectrum. We see that the DMD method is able to isolate the wave energy and flatten the turbulence spectrum under the wave peak. While the wave spectrum contains nonzero energy in the frequencies outside the wave range, the energy is small enough to not affect the turbulence spectrum.

In Fig. 2c, we present a portion of the separated time series over the raw signal. This portion of data was chosen to highlight a potentially difficult section to decompose where the wave amplitude sharply decreases over time. We expect the decomposition to perform best when the wave energy is large relative to that of the turbulence. While we see strong agreement with the wave signal during the first half of the plot, we see the mismatch increases once the wave amplitude decreases in the second half of the plot; however, the decomposed wave velocity is still able to capture the transition moderately well and maintain the shape of the waves. When we later compare this decomposition to other methods, we find it has similar performance to the EEMD and SWT methods because this is the dataset with the largest relative wave energy, i.e., it is theoretically the easiest signal to decompose. Additionally, Table 1 indicates that this is the dataset with the highest relative wave intensity $\tilde{u}_{\text{rms}}/u'_{\text{rms}}$ and also the lowest r/n values. This indicates that the wave motion present in the signal can be captured using a smaller number of modes relative to the total rank.

c. *Laboratory data decomposition*

The laboratory data represent a case with weak wave energy relative to the turbulence and, therefore, we expect it

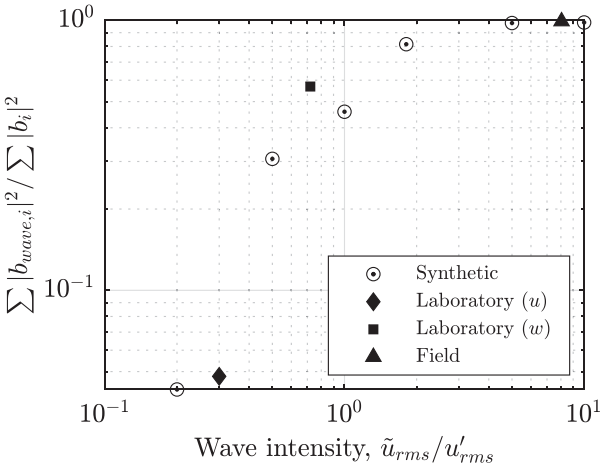

FIG. 7. Relative energy contained in the DMD modes that each wave intensity case requires to resolve the coherent features in the signal. The y axis is the energy of the DMD wave modes relative to the energy contained in the entire signal, where b_i represents the amplitude of the ith DMD mode, while $b_{\text{wave},i}$ represents the amplitude of the subset of DMD modes associated with wave motion and used in the reconstruction of the wave signal.

to be the most challenging to decompose. The data are also more noisy than the field and synthetic data, but it is also the longest dataset of the three. We start by considering the POD spectra of both u and w (Figs. 9a and 10a) which show that the wave energy is contained within the frequency range of 1–3 Hz. What is interesting in these POD spectra, unlike in those of the synthetic and field data, is that the low number modes only contain low-frequency turbulence, and that the wave energy is contained in intermediate modes. Based off the POD spectra, we truncate at $r = 1000$ and $r = 1300$ modes for u and w, respectively.

The fully decomposed spectra are plotted in Figs. 9b and 10b. We see that the DMD method separated and removed most of the wave energy from the turbulence in both cases. First, considering the u spectrum (Fig. 9b), we see that the majority of the wave peak is removed from the turbulence spectrum, and that the wave spectrum has less energy than the turbulence spectrum at almost all frequencies, confirming that this is a turbulence-dominated flow. The time series reconstruction in Fig. 9c again shows the small wave velocity amplitude compared to the turbulence fluctuations. We also see some noise spikes in the data which have been isolated to the turbulence time series.

Next, we consider the w decomposition in Fig. 10b where we observe a cleanly separated turbulence and wave spectra. Note the difference between this and the u spectra, specifically how they have similar wave energy, but the w spectrum has much weaker turbulence. The time series reconstruction in Fig. 10c shows that the separated waves closely follow the trend of the raw data, and that both the high- and low-frequency turbulence fluctuations are isolated to the turbulence time series. In Table 1, we see that this is the dataset with the lowest wave intensity relative to the turbulence. This low wave intensity is a challenge for our decomposition; however, by using a long enough time series and a high r/n truncation, the DMD method is able to give a better separation when compared with other methods.

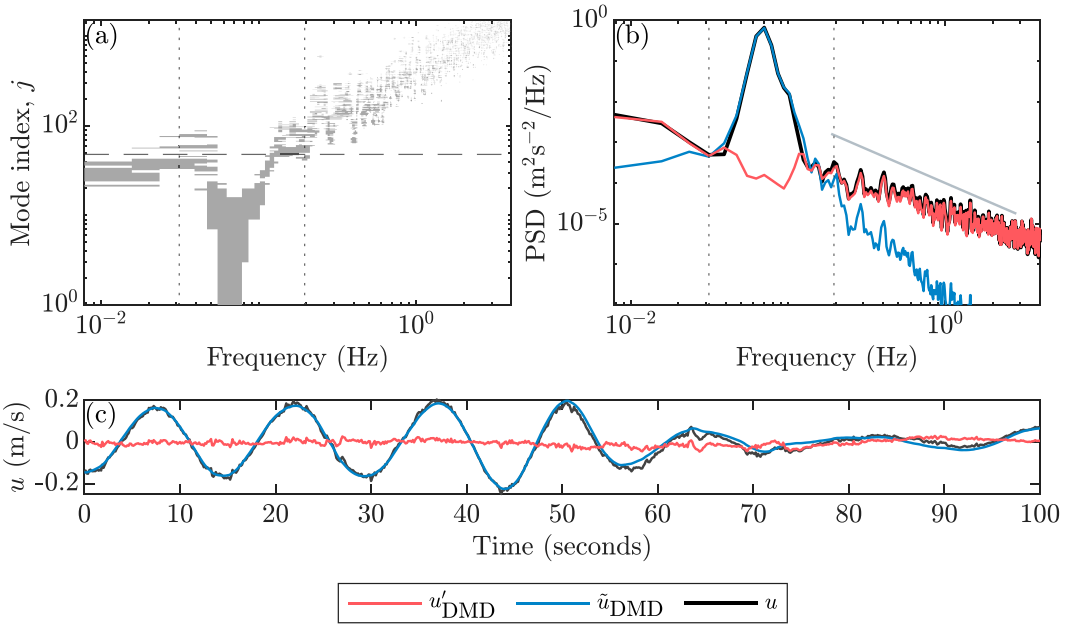

FIG. 8. DMD wave–turbulence decomposition of u-component velocity of field data. (a) POD spectrum of time-delayed matrix **H**. (b) Power spectra of the original data and DMD-separated wave and turbulence. A gray −5/3 slope line is plotted for reference. (c) A portion of the time series of the original and decomposed signals. The wave motion was reconstructed using 34 DMD modes.

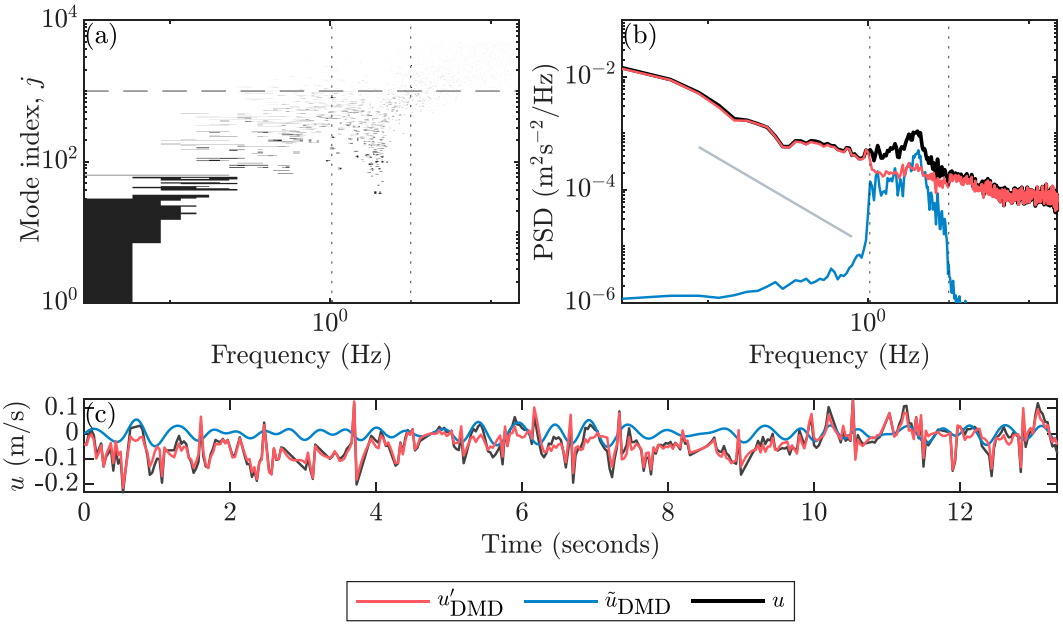

FIG. 9. DMD wave–turbulence decomposition of u-component velocity of laboratory data. (a) POD spectrum of time-delayed matrix **H**. (b) Power spectra of the original data and DMD-separated wave and turbulence. A gray −5/3 slope line is plotted for reference. (c) A portion of the time series of the original and decomposed signals. The wave motion was reconstructed using 506 DMD modes.

To further assess the decomposition results, we compare the mean Reynolds stress $\langle u'w' \rangle$ from the raw signal with those from the decomposed turbulence and wave components. We expect the Reynolds stress associated with waves to be significantly lower than that generated by turbulence. Consistent with this expectation, our analysis shows that the wave Reynolds stress is over an order of magnitude smaller than the residual turbulence Reynolds stress. We find the Reynolds stress values to be -5.1×10^{-4}, -4.5×10^{-4}, and -0.19×10^{-4} $(\text{m s}^{-1})^2$ for the raw, decomposed turbulence,

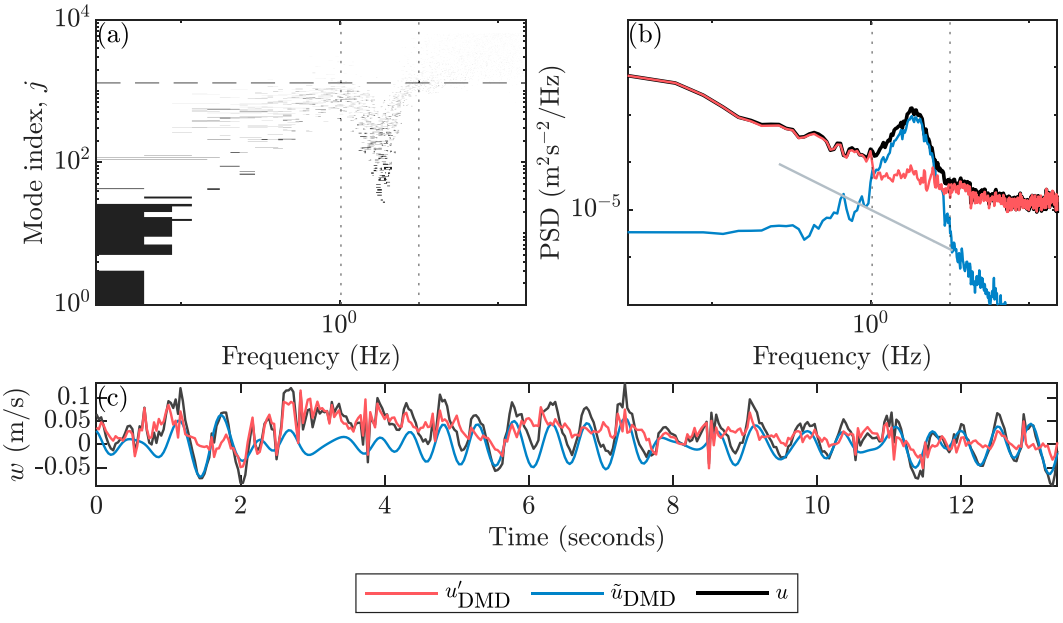

FIG. 10. DMD wave–turbulence decomposition of w-component velocity of laboratory data. (a) POD spectrum of time-delayed matrix **H**. (b) Power spectra of the original data and DMD-separated wave and turbulence. A gray −5/3 slope line is plotted for reference. (c) A portion of the time series of the original and decomposed signals. The wave motion was reconstructed using 732 DMD modes.

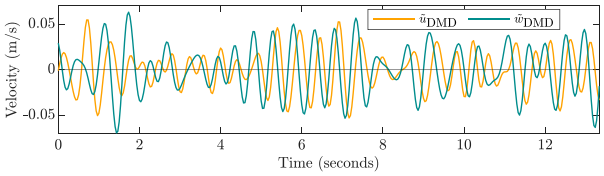

FIG. 11. The u and w velocity components of DMD-separated wave time series of the laboratory data.

and decomposed wave signals, respectively. This confirms that the wave momentum flux is inefficient compared to that of the turbulence, and that the DMD decomposition can successfully isolate wavelike motions from turbulence.

Additionally, we visualize the time series of $\tilde{u}_{\mathrm{DMD}}$ and $\tilde{w}_{\mathrm{DMD}}$ together in Fig. 11. We expect the horizontal and vertical wave velocities to have a 90° phase shift in time and for them to have similar amplitudes given that they were deep-water waves (short waves relative to the depth of the tank). The initial section of Fig. 11 shows a disagreement between both the expected wave magnitudes and the phase shift, which might be caused by the presence of strong turbulence; however, the rest of the time series shows good agreement with the expected wave characteristics from theory. Throughout the time series, the $\tilde{u}_{\mathrm{DMD}}$ velocity amplitude is slightly underpredicted when compared with the $\tilde{w}_{\mathrm{DMD}}$ signal; this is likely due to the u decomposition underperforming due to the stronger turbulence. Overall, we find that the DMD method is able to decompose the signals fairly well, even given a noisy dataset with relatively weak, irregular waves under intermittent wave breaking.

d. *Comparison with other decomposition methods*

We compare our decomposition method to the EEMD and SWT, two other modal decomposition techniques that work with a single time series. To compare the methods, we plot the separated turbulence spectra using each method for each dataset in Fig. 12. Across all four plots, we see that the SWT tends to excessively remove energy from the turbulence in the wave range, causing significant dips in the turbulence spectra. In contrast, the EEMD generally performs as well as the DMD method for the synthetic and field data in Figs. 12a and 12b, respectively. We note that the EEMD has caused some turbulence energy redistribution, e.g., adding energy into the

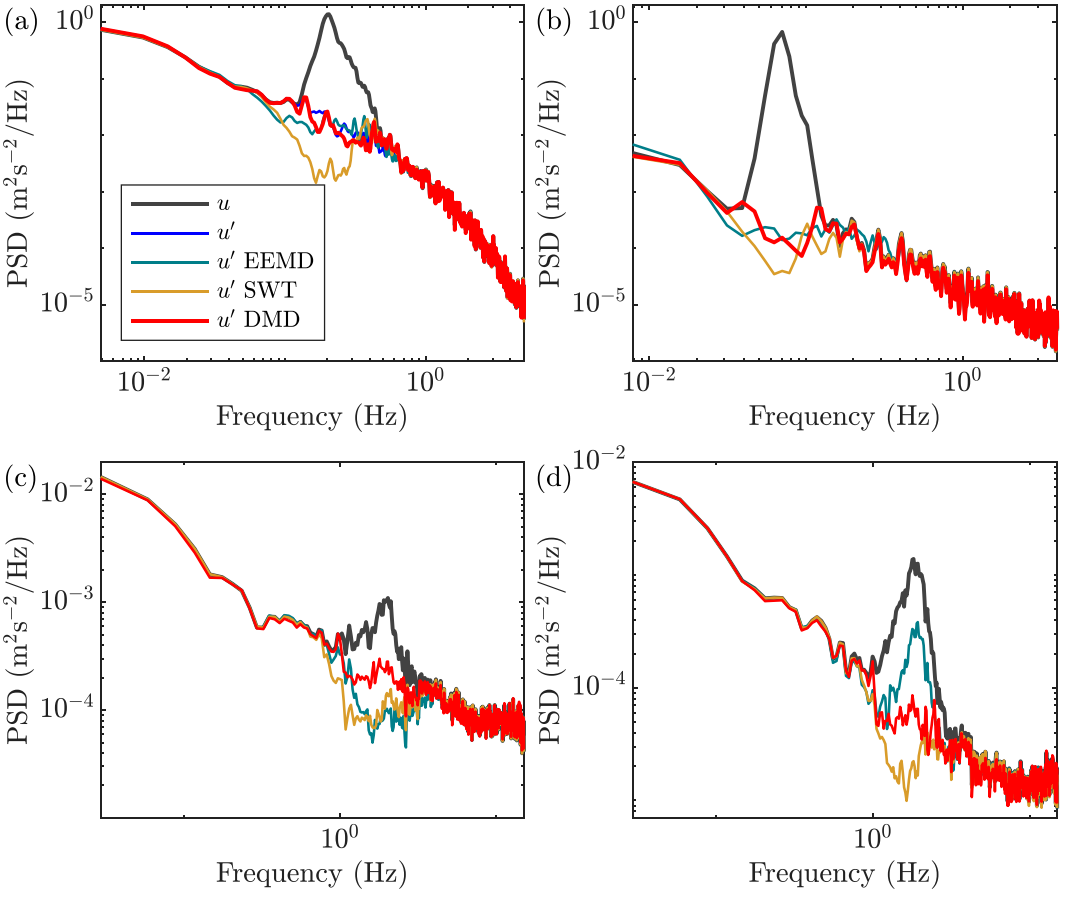

FIG. 12. Comparison of modal decomposition methods, showing the spectra of the original data and the decomposed turbulence data. (a) Synthetic data u velocity, (b) field data u velocity, and (c),(d) laboratory data u and w velocity, respectively.

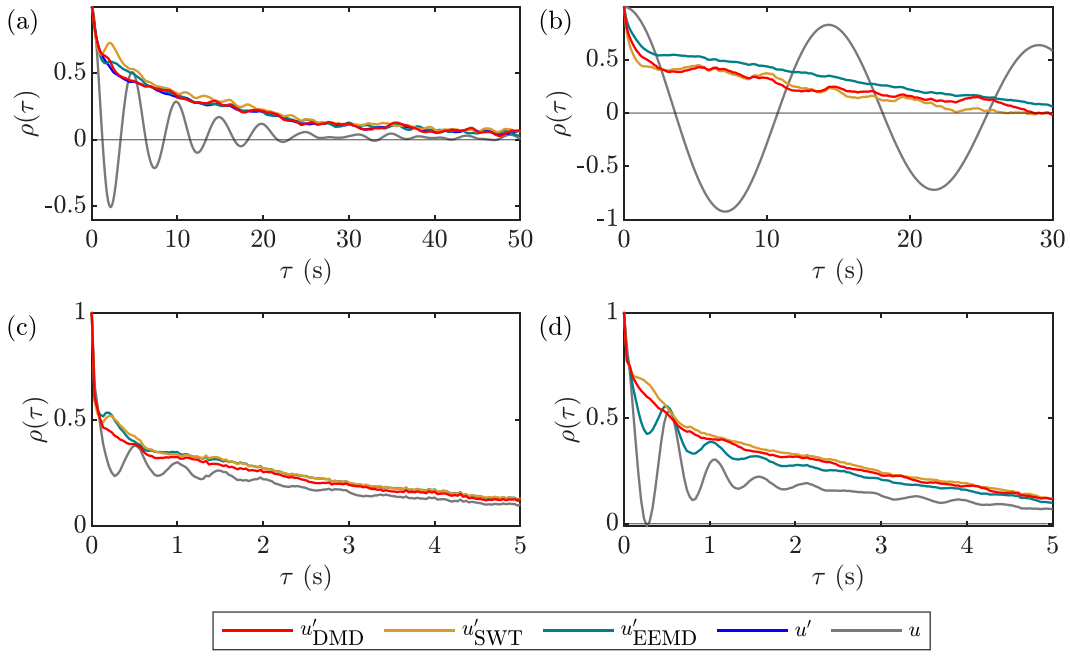

FIG. 13. Normalized autocorrelation of raw u, DMD-filtered turbulence u_{DMD}, EEMD- and SWT-filtered turbulence (u_{EEMD} and u_{SWT}, respectively) signals. (a) Synthetic data u velocity, the black line is the true turbulence u'. (b) Field data u velocity. (c),(d) Laboratory data u and w velocity, respectively.

turbulence in the field data as seen in Fig. 12b between 0.2 and 0.4 Hz. Finally, the laboratory data (Figs. 12c,d) are the hardest to decompose due to its weak, irregular waves, and that is where we clearly see that the DMD outperforms the other two methods. The DMD-filtered spectra are able to closely follow the expected slope of the turbulence spectra for both the u and w velocity spectra.

The methods show the most similar decomposition for the field data, which is the dataset with the highest wave intensity. This is unsurprising and suggests that the stronger the wave intensity, the easier the signal should be to decompose using any method. Even though the synthetic data have exactly no wave–turbulence interactions which should in theory mean it is relatively easy to decompose, its lower wave intensity causes issues for the SWT method. Finally, the laboratory data have the lowest wave intensity, and this is where the benefits of the DMD method are the clearest. One reason the SWT may underperform is because it determines its basis *a priori*; the method tries to fit the data to a wavelet basis, which might not always be a good descriptor of the dynamics of the system. Alternatively, the EEMD uses IMFs as an *a posteriori* basis, that is, they adapt to the data being analyzed. However, it seems that the IMFs might not be separating the waves from the turbulence completely, resulting in mixed modes which contain both turbulence and wave energy. The utility of this method is further hindered by the fact that the number of IMFs is determined by the EEMD algorithm which removes a tuning parameter.

We further compare the methods by computing the normalized autocorrelations $\rho(\tau)$ of the filtered turbulence velocity across the different datasets, as shown in Fig. 13. The raw autocorrelations, plotted in gray for reference, show a clear periodic wave signal across all datasets. Successfully isolating the turbulence from the waves would remove all time periodicity and preserve the exponential decay expected as the turbulence fluctuations decorrelate over time. We see that in most cases, the methods are all able to remove the majority of the wave signal. With respect to the synthetic data (Fig. 13a), we know what the true turbulence signal is, and we see that while all the methods follow the true turbulence autocorrelation (shown with a blue line) closely, the SWT performs the worst, as shown by the small peak in the signal after the initial decrease. In Fig. 13b, the field data autocorrelations all remove the wave, and it is unclear which performs best here from visual inspection. Recall that the EEMD method had added energy into the turbulence spectra, so it is likely that its higher autocorrelation values are inaccurate. Finally, in the laboratory data (Figs. 13c,d), we clearly see the DMD method performs the best. It is able to remove all wave peaks while still capturing the long-time temporal decorrelation of the turbulence. This analysis clearly shows the strength of the DMD method across a variety of datasets and demonstrates how it can be used for more than just spectral analysis, particularly under conditions that pose challenges to other decomposition methods.

6. Conclusions

While many wave–turbulence decomposition methods have been developed over the years, they are typically limited in

their use case. For example, they may be restricted to the spectral domain precluding a time series construction, they may require multiple synchronized measurements, or they may have restrictive assumptions such as no wave–turbulence interactions. In many scenarios, this assumption can easily break, especially because waves and turbulence do interact across different time scales (Guo and Shen 2013). Given these challenges, newer modal decomposition methods have been developed, such as the EEMD and the SWT. These methods still have their drawbacks. For example, the SWT uses a predetermined basis to project the data that is not flexible for highly nonlinear data, whereas the EEMD introduces noise as a filter to differentiate scales in the time series which can result in artificial shifts in how the energy is distributed among the modes.

These approaches are not optimal for highly nonlinear data, resulting in either poor or excessive wave energy separation. To address these limitations, we developed a new wave–turbulence decomposition method using DMD, leveraging its data-driven adaptive basis and minimal assumptions. Our method applies DMD to a single time series, assisted by a time-delay embedding. It is able to isolate the wave components without significantly affecting the turbulent signal at similar frequencies. In the case of velocity data, we show how the method is able to recover the inertial range scaling below the wave peak. The main assumptions that underlie this method are that the waves and turbulence can be separated and that waves are the most coherent feature of the time series, which are reasonable assumptions considering the dynamics of the system. We applied our method to synthetic, field, and laboratory data which covered a range of wave intensities. Our method clearly outperformed the SWT and EEMD when applied to the synthetic and laboratory data, whereas all methods performed similarly when applied to the field data. This may be due to the fact that the field data had the largest wave intensity and, therefore, the wave motion was relatively easy to isolate from the turbulence across all of the methods. A sensitivity analysis on the effect of wave intensity shows that the DMD method performs best when the wave energy is equal to or greater than that of the turbulence. And given that the decomposition relies on isolating the coherent wave motion, the decomposition performs the worst for low wave intensity because the method is unable to identify the wave motion once it is overshadowed by stronger turbulence fluctuations.

The proposed method does require some manual tuning: specifically, the user needs to input the shape of the time-delay matrix, the rank truncation, and the wave frequency range of interest. However, we argue that the parameters are physically related to the signal, especially compared to other methods such as the SWT and EEMD which have somewhat arbitrary tuning parameters. The rank truncation is discernible in the POD spectrum of the time-delayed input matrix, and the wave frequency range is clearly visible in the power spectrum of the signal. While the number of time delays is less clear, our sensitivity analysis shows that it is not as important to the accuracy of the decomposition, especially when the time series length is long enough. We recommend future work to examine this parameter more closely and relate it directly to the wave spectrum. The reported parameters in Table 1 can be a starting point for users of the method. Overall, the proposed DMD-based decomposition method is successful at decomposing wave and turbulence motion with minimal tuning and only one component of data, which is valuable for time series measurements of flow parameters.

We have demonstrated that DMD is powerful for this application, and some fine tuning may need to occur as it is adopted for this and other problems. Future work can focus on more robust DMD schemes and alternative ways of determining the number of modes necessary to reconstruct the wave motion. A few examples include the extended DMD (Williams et al. 2015) which attempts to circumvent certain constraints of the (linear) DMD technique when decomposing data from nonlinear systems, and sparsity-promoting DMD (Jovanović et al. 2014) that can reduce the complexity of the calculations by identifying a smaller set of more relevant DMD modes.

Acknowledgments. We thank Steve Brunton and Caroline Cardinale for helpful comments and insights. We acknowledge support from the U.S. National Science Foundation under Grant CBET-2237550 and the Link Foundation Ocean Engineering and Instrumentation Ph.D. Fellowship. All authors declare that they have no conflicts of interest.

Data availability statement. The field data analyzed in this article are available in Reimers and Fogaren (2021) and its supplemental materials. The synthetic and laboratory data that support the findings of this article, as well as the software used for the analysis, are openly available at https://github.com/DiBenedettoLab/Wave-Turbulence_DMD.

REFERENCES

Albidah, A. B., W. Brevis, V. Fedun, I. Ballai, D. B. Jess, M. Stangalini, J. Higham, and G. Verth, 2021: Proper orthogonal and dynamic mode decomposition of sunspot data. *Philos. Trans. Roy. Soc.*, **A379**, 20200181, https://doi.org/10.1098/rsta.2020.0181.

Araya, D. B., T. Colonius, and J. O. Dabiri, 2017: Transition to bluff-body dynamics in the wake of vertical-axis wind turbines. *J. Fluid Mech.*, **813**, 346–381, https://doi.org/10.1017/jfm.2016.862.

Aubry, N., P. Holmes, J. L. Lumley, and E. Stone, 1988: The dynamics of coherent structures in the wall region of a turbulent boundary layer. *J. Fluid Mech.*, **192**, 115–173, https://doi.org/10.1017/S0022112088001818.

Baker, L., and M. DiBenedetto, 2023: Large-scale particle shadow tracking and orientation measurement with collimated light. *Exp. Fluids*, **64**, 52, https://doi.org/10.1007/s00348-023-03578-y.

Benilov, A. Y., O. A. Kouznetsov, and G. N. Panin, 1974: On the analysis of wind wave-induced disturbances in the atmospheric turbulent surface layer. *Bound.-Layer Meteor.*, **6**, 269–285, https://doi.org/10.1007/BF00232489.

Bian, C., Z. Liu, Y. Huang, L. Zhao, and W. Jiang, 2018: On estimating turbulent Reynolds stress in wavy aquatic environment. *J. Geophys. Res. Oceans*, **123**, 3060–3071, https://doi.org/10.1002/2017JC013230.

Braud, C., D. Heitz, G. Arroyo, L. Perret, J. Delville, and J.-P. Bonnet, 2004: Low-dimensional analysis, using POD, for two mixing layer–wake interactions. *Int. J. Heat Fluid Flow*, **25**, 351–363, https://doi.org/10.1016/j.ijheatfluidflow.2004.02.005.

Bricker, J. D., and S. G. Monismith, 2007: Spectral wave–turbulence decomposition. *J. Atmos. Oceanic Technol.*, **24**, 1479–1487, https://doi.org/10.1175/JTECH2066.1.

Castro, I. P., and C. Vanderwel, 2021: *Turbulent Flows: An Introduction.* IOP Publishing, 200 pp.

Cowherd, M., G. Egan, S. Monismith, and O. Fringer, 2021: Phase-resolved wave boundary layer dynamics in a shallow estuary. *Geophys. Res. Lett.*, **48**, e2020GL092251, https://doi.org/10.1029/2020GL092251.

Daubechies, I., J. Lu, and H.-T. Wu, 2011: Synchrosqueezed wavelet transforms: An empirical mode decomposition-like tool. *Appl. Comput. Harmonic Anal.*, **30**, 243–261, https://doi.org/10.1016/j.acha.2010.08.002.

Dean, R. G., 1965: Stream function representation of nonlinear ocean waves. *J. Geophys. Res.*, **70**, 4561–4572, https://doi.org/10.1029/JZ070i018p04561.

Doron, P., L. Bertuccioli, J. Katz, and T. R. Osborn, 2001: Turbulence characteristics and dissipation estimates in the coastal ocean bottom boundary layer from PIV data. *J. Phys. Oceanogr.*, **31**, 2108–2134, https://doi.org/10.1175/1520-0485(2001)031<2108:TCADEI>2.0.CO;2.

Duke, D., D. Honnery, and J. Soria, 2012: Experimental investigation of nonlinear instabilities in annular liquid sheets. *J. Fluid Mech.*, **691**, 594–604, https://doi.org/10.1017/jfm.2011.516.

Durgesh, V., and J. W. Naughton, 2010: Multi-time-delay LSE-POD complementary approach applied to unsteady high-Reynolds-number near wake flow. *Exp. Fluids*, **49**, 571–583, https://doi.org/10.1007/s00348-010-0821-4.

Feddersen, F., and A. J. Williams III, 2007: Direct estimation of the Reynolds stress vertical structure in the nearshore. *J. Atmos. Oceanic Technol.*, **24**, 102–116, https://doi.org/10.1175/JTECH1953.1.

Filho, E. V., and P. Lopes dos Santos, 2019: A dynamic mode decomposition approach with Hankel blocks to forecast multichannel temporal series. *IEEE Control Syst. Lett.*, **3**, 739–744, https://doi.org/10.1109/LCSYS.2019.2917811.

Foster, D. L., 1997: Dynamics of the nearshore wave bottom boundary layer. Ph.D. thesis, Oregon State University, 129 pp., https://ir.library.oregonstate.edu/concern/graduate_thesis_or_dissertations/p2676z075.

Fujii, K., N. Takeishi, B. Kibushi, M. Kouzaki, and Y. Kawahara, 2019: Data-driven spectral analysis for coordinative structures in periodic human locomotion. *Sci. Rep.*, **9**, 16755, https://doi.org/10.1038/s41598-019-53187-1.

Gerbi, G. P., J. H. Trowbridge, J. B. Edson, A. J. Plueddemann, E. A. Terray, and J. J. Fredericks, 2008: Measurements of momentum and heat transfer across the air–sea interface. *J. Phys. Oceanogr.*, **38**, 1054–1072, https://doi.org/10.1175/2007JPO3739.1.

Gordeyev, S. V., and F. O. Thomas, 2013: A Temporal Proper Decomposition (TPOD) for closed-loop flow control. *Exp. Fluids*, **54**, 1477, https://doi.org/10.1007/s00348-013-1477-7.

Goring, D. G., and V. I. Nikora, 2002: Despiking acoustic Doppler velocimeter data. *J. Hydraul. Eng.*, **128**, 117–126, https://doi.org/10.1061/(ASCE)0733-9429(2002)128:1(117).

Grilli, M., P. J. Schmid, S. Hickel, and N. A. Adams, 2012: Analysis of unsteady behaviour in shockwave turbulent boundary layer interaction. *J. Fluid Mech.*, **700**, 16–28, https://doi.org/10.1017/jfm.2012.37.

Guo, X., and L. Shen, 2013: Numerical study of the effect of surface waves on turbulence underneath. Part 1. Mean flow and turbulence vorticity. *J. Fluid Mech.*, **733**, 558–587, https://doi.org/10.1017/jfm.2013.451.

Hasselmann, K., and Coauthors, 1973: Measurements of wind-wave growth and swell decay during the Joint North Sea Wave Project (JONSWAP). Ergaenzungsheft Zur Deutschen Hydrographischen Zeitschrift, Reihe A 12, 94 pp., http://resolver.tudelft.nl/uuid:f204e188-13b9-49d8-a6dc-4fb7c20562fc.

Heidt, L., and T. Colonius, 2023: Spectral proper orthogonal decomposition of harmonically forced turbulent flows. arXiv, 2305.05628v1, https://doi.org/10.48550/arXiv.2305.05628.

Huang, N. E., and Z. Wu, 2008: A review on Hilbert-Huang Transform: Method and its applications to geophysical studies. *Rev. Geophys.*, **46**, RG2006, https://doi.org/10.1029/2007RG000228.

——, and Coauthors, 1998: The empirical mode decomposition and the Hilbert spectrum for nonlinear and non-stationary time series analysis. *Proc. Roy. Soc. London*, **454A**, 903–995, https://doi.org/10.1098/rspa.1998.0193.

Huang, Y., F. G. Schmitt, Z. Lu, and Y. Liu, 2009: Analysis of daily river flow fluctuations using empirical mode decomposition and arbitrary order Hilbert spectral analysis. *J. Hydrol.*, **373**, 103–111, https://doi.org/10.1016/j.jhydrol.2009.04.015.

Jiang, J.-Y., R. L. Street, and S. P. Klotz, 1990: A study of wave-turbulence interaction by use of a nonlinear water wave decomposition technique. *J. Geophys. Res.*, **95**, 16 037–16 054, https://doi.org/10.1029/JC095iC09p16037.

Jovanović, M. R., P. J. Schmid, and J. W. Nichols, 2014: Sparsity-promoting dynamic mode decomposition. *Phys. Fluids*, **26**, 024103, https://doi.org/10.1063/1.4863670.

Kutz, J. N., S. L. Brunton, B. W. Brunton, and J. L. Proctor, 2016: *Dynamic Mode Decomposition: Data-Driven Modeling of Complex Systems.* Society for Industrial and Applied Mathematics, 250 pp.

Li, G., G. Weiss, M. Mueller, S. Townley, and M. R. Belmont, 2012: Wave energy converter control by wave prediction and dynamic programming. *Renewable Energy*, **48**, 392–403, https://doi.org/10.1016/j.renene.2012.05.003.

Lumley, J. L., 1967: The structure of inhomogeneous turbulent flows. *Atmospheric Turbulence and Radio Wave Propagation*, A. M. Yaglom and V. I. Tartarsky, Eds., Defense Technical Information Center, 166–178.

——, 2007: *Stochastic Tools in Turbulence.* Dover Publications, 194 pp.

Lydon, B., B. Polagye, and S. Brunton, 2025: Data-driven modeling of an oscillating surge wave energy converter using dynamic mode decomposition. *J. Renewable Sustain. Energy*, **17**, 024703, https://doi.org/10.1063/5.0227543.

Magnaudet, J., and L. Thais, 1995: Orbital rotational motion and turbulence below laboratory wind water waves. *J. Geophys. Res.*, **100**, 757–771, https://doi.org/10.1029/94JC02715.

Massa, L., R. Kumar, and P. Ravindran, 2012: Dynamic mode decomposition analysis of detonation waves. *Phys. Fluids*, **24**, 066101, https://doi.org/10.1063/1.4727715.

Perez, L., R. Cossu, C. Couzi, and I. Penesis, 2020: Wave-turbulence decomposition methods applied to tidal energy site assessment. *Energies*, **13**, 1245, https://doi.org/10.3390/en13051245.

Qiao, F., Y. Yuan, J. Deng, D. Dai, and Z. Song, 2016: Wave–turbulence interaction-induced vertical mixing and its effects in ocean and climate models. *Philos. Trans. Roy. Soc.*, **A374**, 20150201, https://doi.org/10.1098/rsta.2015.0201.

Reimers, C. E., and K. E. Fogaren, 2021: Bottom boundary layer oxygen fluxes during winter on the Oregon shelf. *J. Geophys.*

Res. Oceans, **126**, e2020JC016828, https://doi.org/10.1029/2020JC016828.

Rosa, T. L., A. M. Piecho-Santos, R. Vettor, and C. Guedes Soares, 2021: Review and prospects for autonomous observing systems in vessels of opportunity. *J. Mar. Sci. Eng.*, **9**, 366, https://doi.org/10.3390/jmse9040366.

Rowley, C. W., I. Mezić, S. Bagheri, P. Schlatter, and D. S. Henningson, 2009: Spectral analysis of nonlinear flows. *J. Fluid Mech.*, **641**, 115–127, https://doi.org/10.1017/S0022112009992059.

Scherl, I., B. Strom, J. K. Shang, O. Williams, B. L. Polagye, and S. L. Brunton, 2020: Robust principal component analysis for modal decomposition of corrupt fluid flows. *Phys. Rev. Fluids*, **5**, 054401, https://doi.org/10.1103/PhysRevFluids.5.054401.

Schmidt, O. T., and T. Colonius, 2020: Guide to spectral proper orthogonal decomposition. *AIAA J.*, **58**, 1023–1033, https://doi.org/10.2514/1.J058809.

Schmid, P. J., 2010: Dynamic mode decomposition of numerical and experimental data. *J. Fluid Mech.*, **656**, 5–28, https://doi.org/10.1017/S0022112010001217.

——, 2011: Application of the dynamic mode decomposition to experimental data. *Exp. Fluids*, **50**, 1123–1130, https://doi.org/10.1007/s00348-010-0911-3.

——, 2022: Dynamic mode decomposition and its variants. *Annu. Rev. Fluid Mech.*, **54**, 225–254, https://doi.org/10.1146/annurev-fluid-030121-015835.

Seena, A., and H. J. Sung, 2011: Dynamic mode decomposition of turbulent cavity flows for self-sustained oscillations. *Int. J. Heat Fluid Flow*, **32**, 1098–1110, https://doi.org/10.1016/j.ijheatfluidflow.2011.09.008.

Semeraro, O., G. Bellani, and F. Lundell, 2012: Analysis of time-resolved PIV measurements of a confined turbulent jet using POD and Koopman modes. *Exp. Fluids*, **53**, 1203–1220 https://doi.org/10.1007/s00348-012-1354-9.

Shaw, W. J., and J. H. Trowbridge, 2001: The direct estimation of near-bottom turbulent fluxes in the presence of energetic wave motions. *J. Atmos. Oceanic Technol.*, **18**, 1540–1557, https://doi.org/10.1175/1520-0426(2001)018<1540:TDEONB>2.0.CO;2.

Sirovich, L., 1987a: Turbulence and the dynamics of coherent structures. I. Coherent structures. *Quart. Appl. Math.*, **45**, 561–571, https://doi.org/10.1090/qam/910462.

——, 1987b: Turbulence and the dynamics of coherent structures. II. Symmetries and transformations. *Quart. Appl. Math.*, **45**, 573–582, https://doi.org/10.1090/qam/910463.

——, 1987c: Turbulence and the dynamics of coherent structures. III. Dynamics and scaling. *Quart. Appl. Math.*, **45**, 583–590, https://doi.org/10.1090/qam/910464.

Smith, S. R., and Coauthors, 2019: Ship-based contributions to global ocean, weather, and climate observing systems. *Front. Mar. Sci.*, **6**, 434, https://doi.org/10.3389/fmars.2019.00434.

Smyth, C., A. E. Hay, and L. Zedel, 2002: Coherent Doppler Profiler measurements of near-bed suspended sediment fluxes and the influence of bed forms. *J. Geophys. Res.*, **107**, 3105, https://doi.org/10.1029/2000JC000760.

Takens, F., 1981: Detecting strange attractors in turbulence. *Dynamical Systems and Turbulence, Warwick 1980*, D. Rand and L.-S. Young, Eds., Lecture Notes in Mathematics, Vol. 898, Springer, 366–381.

Thais, L., and J. Magnaudet, 1995: A triple decomposition of the fluctuating motion below laboratory wind water waves. *J. Geophys. Res.*, **100**, 741–755, https://doi.org/10.1029/94JC02714.

——, and ——, 1996: Turbulent structure beneath surface gravity waves sheared by the wind. *J. Fluid Mech.*, **328**, 313–344, https://doi.org/10.1017/S0022112096008749.

Thakur, G., E. Brevdo, N. S. Fučkar, and H.-T. Wu, 2013: The synchrosqueezing algorithm for time-varying spectral analysis: Robustness properties and new paleoclimate applications. *Signal Process.*, **93**, 1079–1094, https://doi.org/10.1016/j.sigpro.2012.11.029.

Towne, A., O. T. Schmidt, and T. Colonius, 2018: Spectral proper orthogonal decomposition and its relationship to dynamic mode decomposition and resolvent analysis. *J. Fluid Mech.*, **847**, 821–867, https://doi.org/10.1017/jfm.2018.283.

Trowbridge, J. H., 1998: On a technique for measurement of turbulent shear stress in the presence of surface waves. *J. Atmos. Oceanic Technol.*, **15**, 290–298, https://doi.org/10.1175/1520-0426(1998)015<0290:OATFMO>2.0.CO;2.

Tu, J. H., C. W. Rowley, D. M. Luchtenburg, S. L. Brunton, and J. N. Kutz, 2014: On dynamic mode decomposition: Theory and applications. *J. Comput. Dyn.*, **1**, 391–421, https://doi.org/10.3934/jcd.2014.1.391.

Tutkun, M., and W. K. George, 2017: Lumley decomposition of turbulent boundary layer at high Reynolds numbers. *Phys. Fluids*, **29**, 020707, https://doi.org/10.1063/1.4974746.

Williams, J. J., P. S. Bell, and P. D. Thorne, 2003: Field measurements of flow fields and sediment transport above mobile bed forms. *J. Geophys. Res.*, **108**, 3109, https://doi.org/10.1029/2002JC001336.

Williams, M. O., I. G. Kevrekidis, and C. W. Rowley, 2015: A data–driven approximation of the Koopman operator: Extending dynamic mode decomposition. *J. Nonlinear Sci.*, **25**, 1307–1346, https://doi.org/10.1007/s00332-015-9258-5.

Young, D. L., and D. R. Webster, 2018: Assessment of single-instrument techniques for removing wave bias from Reynolds stress estimates. *Limnol. Oceanogr. Methods*, **16**, 35–50, https://doi.org/10.1002/lom3.10225.

Zhu, Q., B. C. van Prooijen, Z. B. Wang, Y. X. Ma, and S. L. Yang, 2016: Bed shear stress estimation on an open intertidal flat using in situ measurements. *Estuarine Coastal Shelf Sci.*, **182**, 190–201, https://doi.org/10.1016/j.ecss.2016.08.028.